Efficient Promoters and Reaction Paths in the CO 2 Hydrogenation to Light Olefins over Zirconia-Supported Iron Catalysts

Alan Barrios, Deizi Peron, Anoop Chakkingal, Achim Iulian Dugulan, Simona Moldovan, Kalthoum Nakouri, Joëlle Thuriot-Roukos, Robert Wojcieszak, Joris Thybaut, Mirella Virginie, et al.

Efficient promoters and reaction paths in the CO2 hydrogenation to light olefins over zirconia supported iron catalysts

Journal:	*ACS Catalysis*
Manuscript ID	cs-2021-05648p.R1
Manuscript Type:	Article
Date Submitted by the Author:	n/a
Complete List of Authors:	Barrios, Alan; Unité de Catalyse et Chimie du Solide Peron, Deizi; Unité de Catalyse et Chimie du Solide Chakkingal, Anoop; University of Ghent Dugulan, Achim Iulian; Technische Universiteit Delft, R3 Reactor Institute Delft Moldovan, Simona; Groupe de Physique des Materiaux Nakouri, Kalthoum; Groupe de Physique des Materiaux Thuriot-Roukos, Joëlle; Université de Lille Faculté des Sciences et Technologies, UCCS-CNRS Wojcieszak, Robert; Centre National de la Recherche Scientifique, Chemistry Thybaut, Joris; Universiteit Gent, Chemical Engineering Virginie, Mirella; Unité de Catalyse et Chimie du Solide Khodakov, Andrei; CNRS, Unité de catalyse et chimie du solide

January 19th, 2022

Efficient promoters and reaction paths in the CO_2 hydrogenation to light olefins over zirconia supported iron catalysts

Alan J. Barrios[a, b], Deizi V. Peron[a], Anoop Chakkingal[a,b], Iulian Dugulan[c], Simona Moldovan[d], Kalthoum Nakouri[d], Joëlle Thuriot-Roukos[a], Robert Wojcieszak[a], Joris W. Thybaut[b], Mirella Virginie[a] and Andrei Y. Khodakov[a]*

[a]*Univ. Lille, CNRS, Centrale Lille, Univ. Artois, UMR 8181 – UCCS – Unité de Catalyse et Chimie du Solide, F-59000 Lille, France*

[b]*Laboratory for Chemical Technology (LCT), Department of Materials, Textiles and Chemical Engineering, Ghent University, Technologiepark 125, B-9052 Ghent, Belgium*

[c]*Fundamental Aspects of Materials and Energy Group, Delft University of Technology, Mekelweg 15, Delft, 2629 JB, Netherlands*

[d]*Groupe de Physique des Matériaux, CNRS, Université Normandie & INSA Rouen Avenue de l'Université - BP12, 76801 St Etienne du Rouvray, France*

Abstract

Hydrogenation into light olefins is an attractive strategy for CO_2 fixation into chemicals. In this paper, high throughput experimentation and extended characterization were employed to identify the most efficient promoters and to elucidate structure-performance correlations and reaction paths in the CO_2 hydrogenation to light olefins over zirconia supported iron catalysts.

K, Cs, Ba, Ce, Nb, Mo, Mn, Cu, Zn, Ga, In, Sn, Sb, Bi, and V added in the same molar concentrations to zirconia supported iron catalyst were evaluated as promoters. The CO_2 hydrogenation proceeds via intermediate formation of CO followed by surface polymerization. Over the iron catalysts containing alkaline promoters, initially higher selectivity to light olefins shows a significant decrease with the CO_2 conversion, because of further surface polymerization and formation of longer chain hydrocarbons. A relatively low selectivity to light olefins over the promoted catalysts, without potassium, is not much affected by the CO_2 conversion.

Essential characteristics of iron catalysts in order to obtain higher yield of light olefins seem to be higher iron dispersion, higher extent of carbidization and optimized basicity. The strongest promoting effect is reported for alkaline metals. A further increase in the light olefin selectivity is observed after simultaneous addition of potassium with copper, molybdenum, gallium or cerium.

Keywords: CO_2 mitigation; hydrogenation; light olefins; iron catalysts; high throughput

1. Introduction

The growing concentration of CO_2 in the atmosphere is the major reason of climate changes. There are currently two strategies for dealing with the ever-increasing levels of CO_2: Carbon Capture and Storage (CCS)[1] and Carbon Capture and Utilization (CCU)[2]. CCS is based on the capture of CO_2 from power plants and industrial facilities including its separation, compression and transport, for permanent storage in a geological layer. CCU involves either direct technological use of CO_2 or its chemical and biological conversion into high value-added products [2–4].

The CO_2 fixation into chemicals is an essential CCU strategy. In this strategy, CO_2 can be considered not only the major pollutant but also a feedstock for synthesis of valuable chemicals and fuels[5,6]. Nevertheless, CO_2 chemical utilization is challenging, because of its thermodynamic stability, resulting in low conversion[7]. With sustainable hydrogen as co-reagent, CO_2 can be hydrogenated[7] to methanol[8–10], dimethyl ether[11–14], formic acid [15,16], higher alcohols [17], liquid hydrocarbon fuels [18,19], aromatics[20] and light olefins[7,21–24]. The light olefin synthesis from CO_2 has attracted particular attention in recent years from both academia and companies, since ethylene, propylene and butylenes are major building blocks in the chemical industry. These compounds are widely used in manufacturing polymers, chemical intermediates and solvents. Currently, light olefins are mainly produced by naphtha thermal cracking[25], dehydrogenation of light alkanes [26] and methanol to olefins (MTO) conversion[27–29]. Recently, novel bifunctional or multifunctional catalysts, which are composed of metal oxide nanoparticles and zeolites have been proposed [22,30–32] for hydrogenation of CO_2 into light olefins via so called “methanol-mediated route”. Lower catalytic activity, higher selectivity to coproduced CO (>60-80%) and insufficient olefin yield (usually less than 7% [31,32]) represent major drawbacks of this approach.

The CO_2 Fischer-Tropsch (CO_2-FT) synthesis, which allows achieving a higher single-pass yield, is a promising route to transform CO_2 into light olefins [33]. The CO_2 conversion into olefins proceeds via a combination of reverse water gas shift reaction (RWGS) and Fischer-Tropsch (FT) synthesis:

RWGS: $CO_2 + H_2 \leftrightarrow CO + H_2O$, $\Delta_R H_{300°C} = +38$ KJ/mol

FT synthesis: $nCO + 2nH_2 \rightarrow C_nH_{2n} + nH_2O$, $\Delta_R H_{300°C} = -165$ KJ/mol

Due to their high activity in both RWGS and FT reactions, iron-based catalysts remain the principal option for the CO_2-FT synthesis. Nonetheless, iron employment by itself does not necessarily result in a sufficiently high light olefin selectivity. The optimization of catalyst chemical composition and structure is therefore required to attain high and selective yield of these products. Most commonly, iron catalysts for CO_2 hydrogenation to light olefins have been supported by oxides or carbon materials. In particular, SiO_2, TiO_2, Al_2O_3, ZrO_2 and carbon materials have been evaluated[34] as supports. Strong hydrophilicity and instability of alumina support could be detrimental for the CO_2 hydrogenation, which may generate larger amounts of water than the CO hydrogenation. Relatively weak hydrophilic character of the support could be one of the required characteristics for the CO_2 hydrogenation catalysts. Among the investigated supports, the ZrO_2-supported catalysts have shown the highest selectivity and yield of light olefins[34]. Recent results suggest[35,36] that higher selectivity to light olefins can be achieved using carbon materials as supports of iron catalysts. Note however, that the stability of carbon-based catalysts can be a problem for industrial applications, since the activation and regeneration of the catalysts usually involve oxidative treatments with air.

The iron CO_2-FT catalysts are most commonly promoted with potassium[34,37–46], Co[47–51], Cu[52,53], Mn [45,46,54] and/or Zn[31,44,55,56]. Much less information is available on promotion with other elements. Note that unambiguous identification of the most efficient promoters for iron CO_2 hydrogenation catalysts seems challenging. First, the iron catalysts prepared and investigated by different research groups may have different contents of promoters. Second, different catalyst activation and reaction procedures even with the same catalyst employed by different groups may lead to different catalytic performance. In this work, we used three groups of promoters for zirconia supported iron catalysts. First, we selected alkali metals, which bring strong basicity[57,58]. Second, we promoted iron catalysts with transition metals which can have multiple oxidation states favoring carbon dioxide activation. Finally, "soldering" metals[59,60] like Bi, Sn and Sb were used for the promotion. They have low melting point that could give them higher mobility[61] on the catalyst surface.

High-throughput experimentation (HTE)[62–65] is a fast, reliable and powerful technique generating a tremendous amount of data and is effective for discovering new catalysts. Recently, the HTE strategy [66] uncovered novel highly efficient promoters such as "soldering metals" (Bi, Pb, Sn and Sb) for high temperature FT synthesis using syngas over iron catalysts.

This paper focuses on the one hand, on the selection of most efficient new promoters for iron catalysts, identification of structure-performance-correlations and on the other hand, on the elucidation of reaction paths in CO_2 hydrogenation over promoted iron catalysts. The promoters were added in the same molar concentrations; the catalysts were activated and tested under the same conditions. The effects of 15 different elements (K, Cs, Ba, Ce, Nb, Mo, Mn, Cu, Zn, Ga, In, Sn, Sb, Bi, and V) on the Fe/ZrO_2 catalyst structure and CO_2 hydrogenation to light olefins were investigated over zirconia supported iron catalysts using HTE catalytic measurements and a large

combination of characterization techniques: XRF, nitrogen adsorption, XRD, TPR, TPD, TGA/DSC, *in-situ* Mössbauer spectrometry, STEM-HAADF and STEM-EDS.

2. Experimental

2.1. Catalyst preparation

Commercial zirconia (Alpha Aesar) was used as catalytic support. Distilled water was used as solvent. In the case of Nb, Sn and Sb, ethanol (Verbiese) was applied, because of the insolubility of those salts in water. The following precursors were used for the promotion of zirconia supported iron catalysts: KNO_3 (Sigma-Aldrich), $CsNO_3$ (Sigma-Aldrich), $Ba(NO_3)_2$ (Sigma-Aldrich), $Ce(NO_3)_3.6H_2O$ (Fluka), $NbCl_5$ (Alfa Aesar), $(NH_4)_6Mo_7O_{24}\cdot 4H_2O$ (Sigma-Aldrich), $Mn(NO_3)_2.4H_2O$ (Sigma-Aldrich), $Cu(NO_3)_2.3H_2O$ (Acros Organics), $Zn(NO_3)_2.6H_2O$ (Sigma-Aldrich), $Ga(NO_3)_3.xH_2O$ (Sigma-Aldrich), $In(NO_3)_3.xH_2O$ (Sigma-Aldrich), $SnCl_2\cdot 2H_2O$ (Sigma-Aldrich), $SbCl_3$ (Sigma-Aldrich), $Bi(NO_3)_3.5H_2O$ (Sigma-Aldrich), NH_4VO_3 (Sigma-Aldrich).

Apart from the Sb-promoted iron catalyst, all the other promoted catalysts were synthesized by single-step co-impregnation method. During the co-impregnation, the precursors of potassium and second promoter are added at the same time. In the case of Sb promoted catalysts, we added first Sb and then potassium. A 0.2 M solution of $Fe(NO_3)_3.9H_2O$ along with the promoter salt was added dropwise to the zirconia support. The concentrations of the impregnating solutions were calculated in order to obtain about 10 wt. % iron in the final catalysts; the atomic ratio of Fe to promoter (M) was 50:1. The nominal concentration of potassium in the catalysts was 1 wt.%. After adding the impregnating solution to ZrO_2, the mixture was stirred for 8 h at room temperature. Next, the solvent was evaporated at 80 °C. Then, the catalysts were dried overnight in an oven at 120 °C.

Finally, they were calcined in air at 500 °C for 5 h with a 1 °C/min temperature ramp. Two different sets of catalysts without and with potassium denominated respectively as FeM/ZrO_2 and FeKM/ZrO_2 were synthesized, where M represents Cs, Ba, Ce, Nb, Mo, Mn, Cu, Zn, Ga, In, Sn, Sb, Bi, or V. The chlorine contents in the catalysts prepared using chlorine-containing precursors ($SbCl_3$ and $NbCl_5$) were measured by FRX. The chlorine contents were relatively low (0.007 wt. %) in FeSb/ZrO_2 and 0.63 wt. % in FeNb/ZrO_2.

2.2. Catalyst characterization

The low temperature N_2 physisorption measurements were carried out on a Micromeritics Tristar II PLUS Surface Area and Porosimetry analyzer. The samples were degassed under vacuum at 120 ºC for 3 h. The nitrogen adsorption-desorption isotherms were measured at -196 ºC. The specific surface area of the samples was calculated by the BET method.

The relative promoter content was determined using an energy dispersive micro-X-ray Fluorescence spectrometer M4 TORNADO (Bruker). The sample irradiation was made using a Rhodium X-ray tube (50 kV/200 mA, 10 W). This X-rays source is equipped with a polycapillary lens enabling excitation of an area of 200 µm. For each sample, 36 points (of 200 µm) were analyzed covering the entire sample surface. The detector used was a Silicon-Drift-Detector Si(Li) with (<145 eV resolution at 100000 cps (Mn Kα)) and cooled with a Peltier cooling (-20 °C). The measurement was done under vacuum (20 mbar). Quantitative analysis was done using fundamental parameters (FP) (standardless). The quantification was made based on the identified element.

For the CO_2 temperature programmed desorption (TPD) experiments, the samples were pretreated at 500°C in He for 1 h, cooled down to 40°C, and exposed to CO_2 for 30 min. Then, the

samples were heated up with the ramping rate of 10°C/min to reach 700°C in He flow. The CO_2 desorption was measured by a TCD detector.

The reduction behavior of the catalysts was evaluated by hydrogen temperature-programmed reduction (TPR) using an AutoChem II 2920 apparatus (Micromeritics). The samples (~0.05 g) were reduced in a flow of 5% H_2/Ar flow (50 mL/min) and heated up to 1000 ºC with the temperature ramp rate of 10 ºC/min.

The samples were characterized by X-ray powder diffraction (XRD) using a Bruker AXS D8 diffractometer with a monochromatic Cu Kα radiation (λ =0.1538 nm). The XRD patterns were collected with the 2θ range between 10 to 90°, using a step size of 0.02° and with an acquisition time of 0.5 s. The identification of crystalline phases present in the catalysts was carried out by comparison with the JCPDS standard software.

To determine the carbon deposition on the catalysts, the thermogravimetric analysis was performed using an SDT Q600 V20.9 Build 20 Thermogravimetric Analyzer (TGA) & Differential Scanning Calorimeter (DSC) with ~10 mg sample, with a temperature ramp of 5 ºC/min up to 600 ºC under air.

The catalysts activated in a flow of CO at 350°C and then passivated in a flow of nitrogen at room temperature were characterized using Scanning Transmission Electron Microscopy (STEM), under the High-Angle Annular Dark- Field imaging (STEM-HAADF) and Energy-Dispersive X-ray Spectroscopy (STEM-EDS) modes. The powder specimens were dispersed in ethanol by ultrasounds, a drop of suspension was deposited on a holey carbon film previously deposited on a 300 mesh TEM Cu grid. The catalysts were analyzed using STEM with a high energy beam of 200 kV and a beam size of <1 Å for the imaging purposes, whereas the chemical maps were carried out by a probe with a diameter of about 1 Å. STEM-HAADF with Z-contrast enabled identification of atoms and atom agglomerations of species associated with heavy

elements. More specific, the heavier is the element, the higher the contrast is. The STEM-EDS mapping allowed the analysis of elemental composition within the samples. The Analytical TEM Jeol-ARM200 Cold FEG microscope with Objective and Probe correctors was used for these investigations. The STEM-EDS maps were acquired on a Jeol Centurio 100 mm^2 detector mounted on the TEM. A scanning speed of 20 µsec/px was employed for imaging within the Digital Migrograph software and 0.05µs/px for STEM-EDS elemental mapping using the Analysis Station software, respectively. The maps size was fixed at 256x256 px with a spatial drift correction every 60 sec. In order to gather maps with high signal to noise ratios, long duration chemical mapping were carried out for durations between 80 and 180 minutes. The elemental maps were used in a first approach to assess qualitatively the presence, distribution and location of the elements of interest and to quantitatively estimate the size of the Fe NPs, in a second time. The size distribution histogram of each sample was conducted based on more than 100 nanoparticles taken from different micrographs acquired in the Digital Micrograph software, whilst the elemental maps acquired in the Analysis Station were employed to asses for the size of Fe particles (measured in the longer direction).

The transmission ^{57}Fe Mössbauer spectra were collected at -153°C with a sinusoidal velocity spectrometer using a ^{57}Co(Rh) source. The velocity calibration was carried out using an α-Fe foil at room temperature. The source and absorbing samples were kept at the same temperature during the measurements. The Mössbauer spectra were fitted using the Mosswinn 4.0 program [67]. The experiments were performed at pressures up to 10 bar, in a state-of-the-art high-pressure Mössbauer *in-situ* cell, which was recently developed at the Reactor Institute of Delft [68]. The high-pressure beryllium windows used in this cell contain 0.08% Fe impurity, whose spectral contribution was fitted and removed from the final spectra.

2.3. Catalytic tests

The catalytic screening tests were performed both in the high throughput experimentation unit (HTE, Flowrence, Avantium) and in a laboratory fixed bed reactor. Further information about the HTE unit is available in Ref. [65]. In the HTE unit, the feed gas is homogeneously split via previously calibrated high pressure-drop capillaries into 16 reactors. One of them filled with the inert support serves as reference. Each four reactors form an independent block, maintained at the same temperature. Any liquid phase (if produced) can be collected at 60 °C, while the remaining gas was subsequently sampled on-line for GC analysis. The catalysts were loaded in a stainless-steel tube with inner diameter of 2.0 mm, length of 15 cm. Both ends (height of 3.5 cm) of the reactor tube were filled with inert SiC (size of 0.105 mm and 0.210 mm), where the catalyst (grain size: 50-100 μm) was loaded in between. Prior to the CO_2 hydrogenation reaction, all catalysts were activated in CO (10 mL/min) under atmospheric pressure at 350 °C for 10 h and cooled to 180 °C. At this temperature, the system was pressurized in H_2/CO_2 (3:1) to 10 bar, temperature was step-wisely (1 °C/min) increased to 350 °C. The catalytic performance was measured under different WHSV (4.67-18.19 L/ g.h) staying for at least 12 h at each space velocity. The gaseous products were analyzed online using gas chromatography (GC). Permanent gases (He, H_2, O_2, N_2, CH_4, and CO) were separated by a Hayesep Q/Molecular Sieve column and determined by a thermal conductivity detector (TCD). CO_2 and C_2-C_4 hydrocarbons were separated and measured by a PPQ/PPQ column and TCD, while the C_5-C_{12} hydrocarbons by a CP-Sil5/CP-Sil5 column and a flame ionization detector (FID), respectively. The HTE unit is equipped with a 16 ways-valve system that allows the injection of the gases coming from each reactor one by one in a sequence mode. Also, the program used for gas analysis with GC was optimized and lasts a total of 12 min. The conversion and selectivity calculations are given in **Supporting Information** (**SI**). The carbon balance was better than 92%.

In addition to HTE tests, the catalytic behavior of several promoted ZrO_2-supported iron catalysts was also measured in a laboratory fixed-bed reactor with the 2 mm internal diameter, length 15 cm. Both ends of the reactor tube were filled with inert SiC (size of 0.500 mm), where ~110 mg of fresh catalyst (grain size: 50-100 μm) has been loaded into the reactor. The catalysts were activated in CO under atmospheric pressure with a heating ramp of 2 ºC/min until reaching the reaction temperature of 350 ºC and dwelling at that temperature for 10 h under CO flow (10 mL/min). After cooling down to 180 ºC, a gas mixture composed of $H_2/CO_2 = 3$ was fed into the reactor. Nitrogen with a flow of 1 cm^3/min was used as internal standard for the calculation of CO_2 conversion. After the flow rates and the pressure have been stabilized, the temperature was increased up to 350 ºC with a heating ramp of 1 ºC/min to start the reaction. For the analysis of reagents and reaction products, a Varian CP-3800 chromatograph equipped with a TCD and a FID detectors was used. Two columns were used for this analysis, the first is a packed CTR-1 column connected to the TCD detector, and the second one is an Rt-Q-PLOT capillary column connected to the FID detector. There was no production of liquid phase.

Iron time yields (FTY) were expressed as moles of CO_2 converted per gram of iron (determined from XRF) per second. The Turnover Frequency (TOF) values were calculated[69] using the density of Hägg iron carbide Fe_5C_2 ($\rho = 7.57$ g/cm^3) and assuming 14 Fe atoms/nm^2. The CO-free hydrocarbon selectivities on carbon basis were calculated taking into account only hydrocarbon production in the CO_2 hydrogenation.

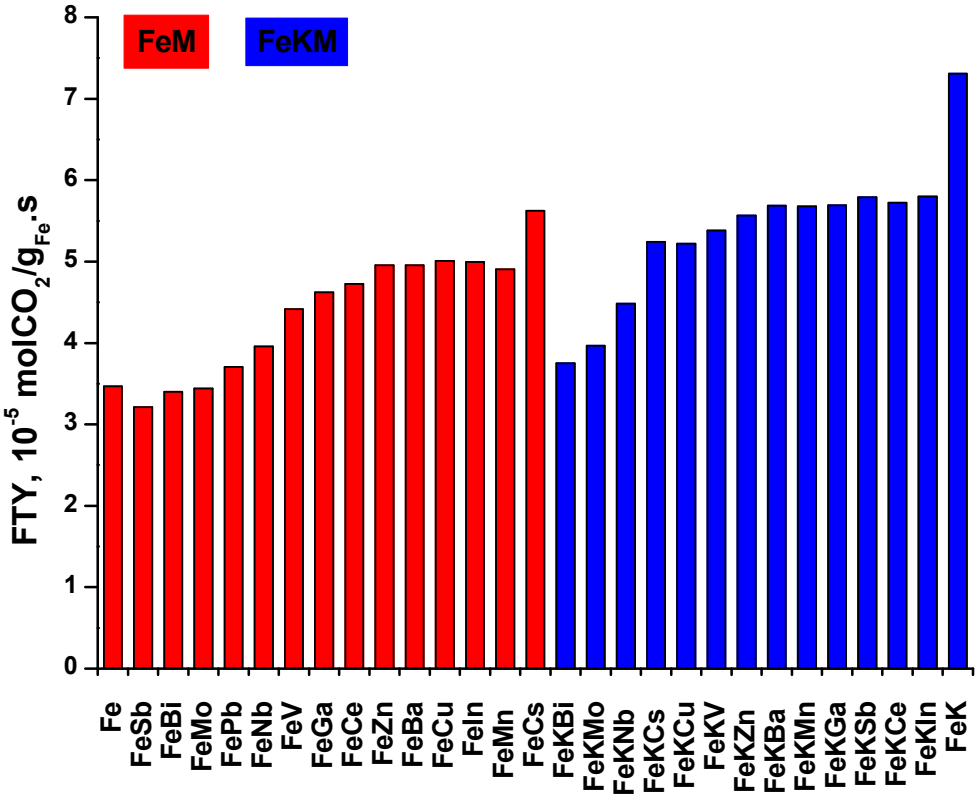

Figure 1. Carbon dioxide conversions and iron time yields (FTY) measured over the promoted zirconia supported iron catalysts T=350 °C, $H_2/CO=3$, p=10 bar, TOS = 50 h.

3. Results

3.1. HTE evaluation of the promoted iron catalysts

3.1.1. Catalyst activity and iron time yield

Carbon dioxide hydrogenation reaction ($H_2/CO_2=3$, P=10 bar, T=350 °C) yielded CO, methane, C_2-C_4 paraffins, olefins and C_{5+} hydrocarbons (until C_{12}). There was no evidence of oxygenated compounds or long-chain liquid hydrocarbons. The CO_2 conversions in the range from 25 to 45 % were obtained by adjusting the gas-space velocity. This conversion range allowed accurate measurements of the overall CO_2 hydrogenation rates and product selectivities. The catalytic activity is expressed as iron time yield for each catalyst (**Figure 1)**. Note that the promotion with Sb, Bi, and Mo seems to have a slightly negative effect on the catalyst activity. All other promoted

catalysts exhibited higher activities than the reference unpromoted Fe/ZrO_2. The most pronounced increase in the reaction rate was observed over the potassium and cesium promoted catalysts. The iron time yield almost doubled after addition of 1.5 wt. % of potassium. Interestingly, the combined promotion with potassium and a second element generally led to higher reaction rates, compared to the promotion without potassium.

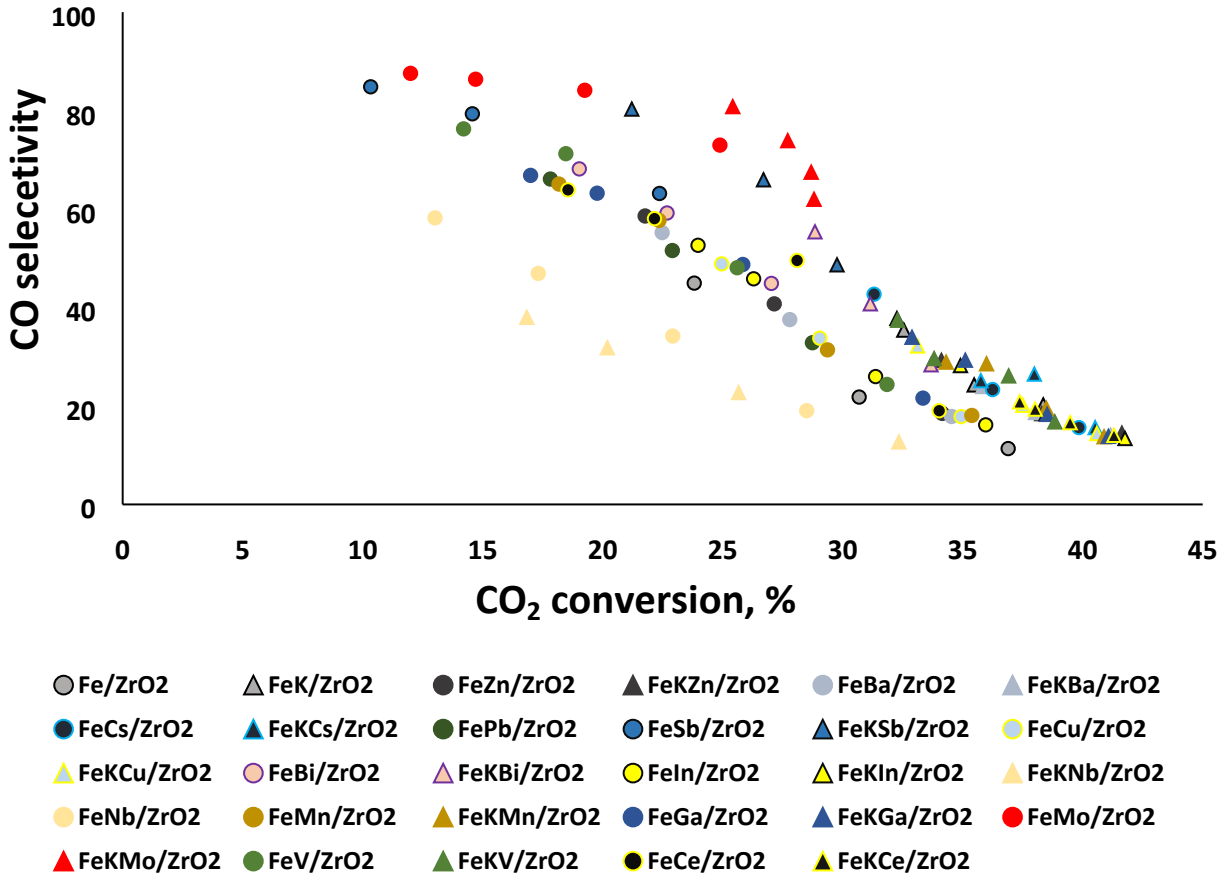

Figure 2. CO selectivity versus carbon dioxide conversion for the Fe/ZrO_2 promoted catalysts. T=350°C, H_2/CO=3, WHSV=4.67-18.19 L/ g.h, P=10 bar, TOS = 50 h.

3.1.2. Product selectivity at different conversions

The selectivities of CO_2 hydrogenation to carbon monoxide and hydrocarbons measured at different WHSV are shown in **Figures 2-6**. At lower CO_2 conversions, the selectivity to CO is very high; the extrapolation of CO selectivity to the zero CO_2 conversion yields almost 100%. The CO

selectivity decreases as a function of CO_2 conversion (**Figure 2**). The CO selectivity drops to 10% at the CO_2 conversions exceeding 40%. Carbon monoxide seems to be produced by RWGS. Extremely high CO selectivity (>90%) at low CO_2 conversion and extrapolation to 100% at zero CO_2 conversion suggest that CO is the primary product of CO_2 hydrogenation over iron catalysts. Thus, the CO_2-FT synthesis proceeds *via* intermediate formation of carbon monoxide.

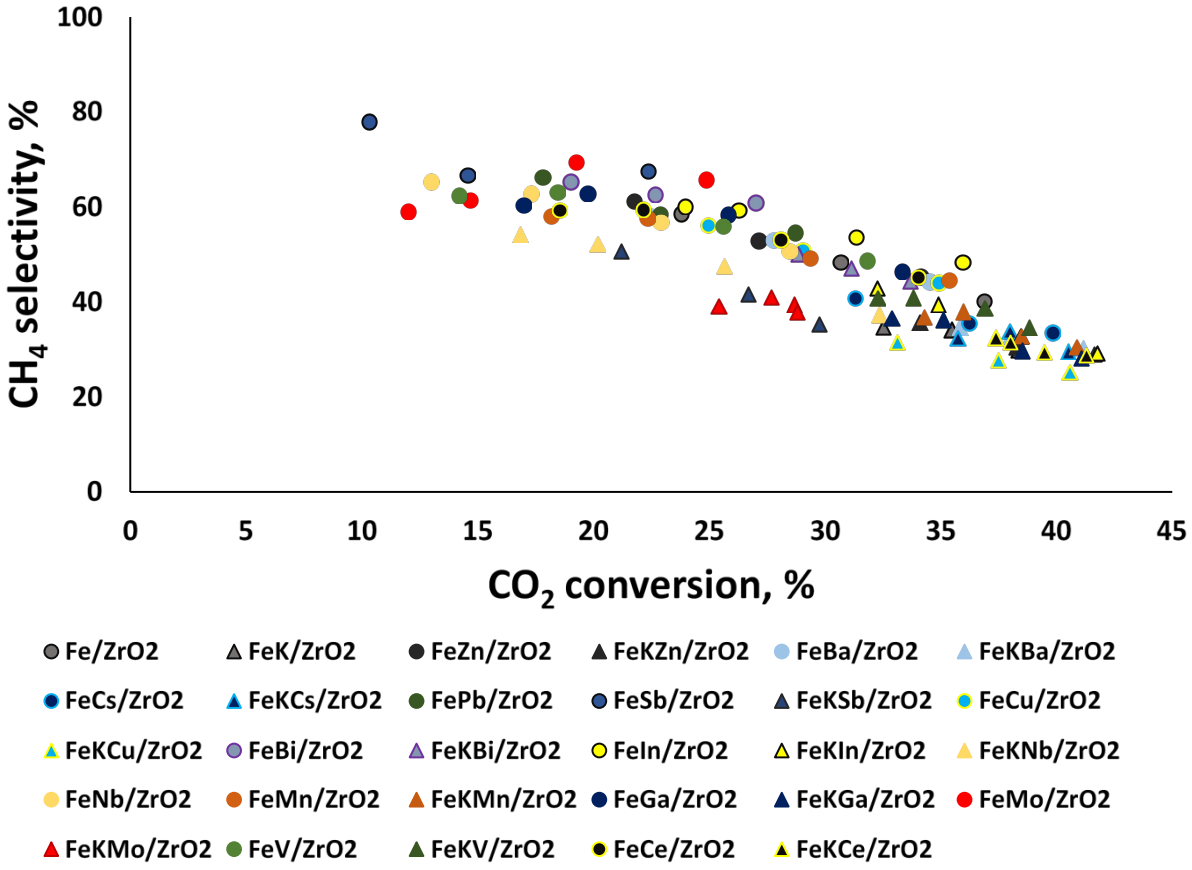

Figure 3. Methane selectivity versus carbon dioxide conversion for Fe/ZrO_2 promoted catalysts. T=350°C, H_2/CO=3, WHSV=4.67-18.19 L/ g.h, P=10 bar, TOS = 50 h.

Note that the CO selectivity at the same conversion varies for different catalysts. The CO selectivity was particularly high over the antimony and molybdenum promoted catalysts, while a somewhat lower CO selectivity was observed over the niobium promoted samples. Interestingly, the promoted iron catalysts containing potassium show higher CO selectivity at the same conversion (except for

the catalyst promoted with Nb), compared to the promoted iron catalysts without potassium (**Figure 2**).

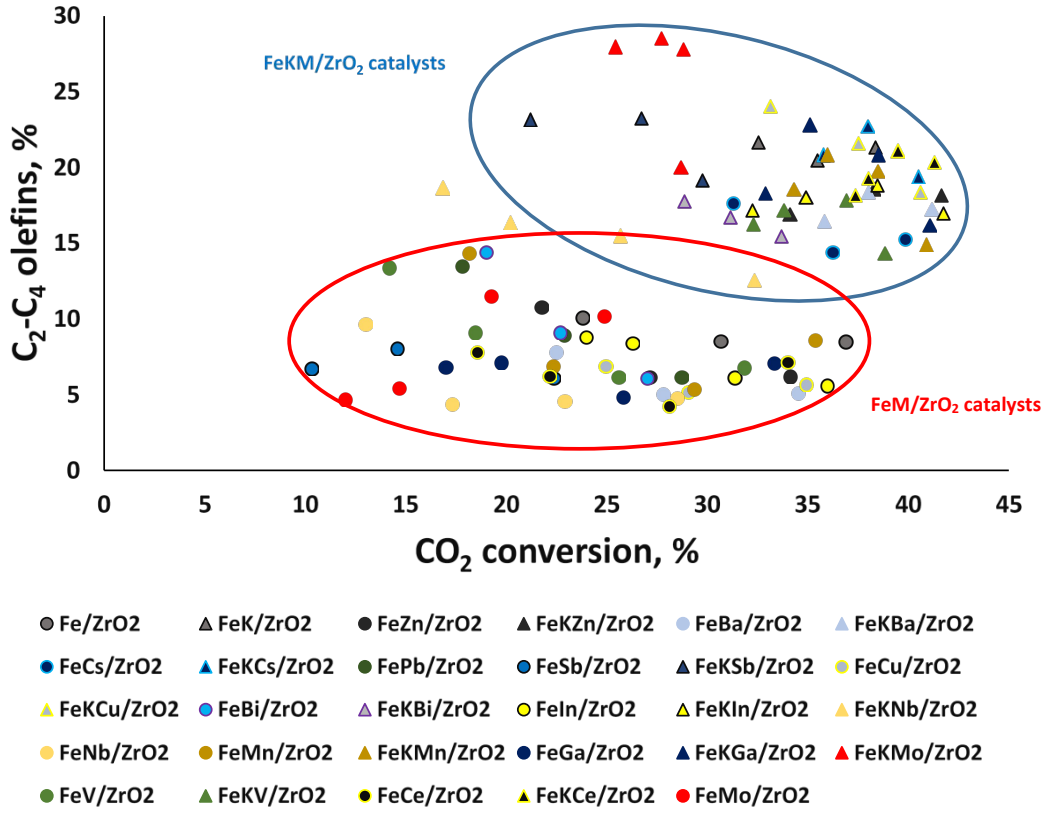

Figure 4. Light olefin selectivity versus carbon dioxide conversion for Fe/ZrO_2 promoted catalysts. T=350°C, H_2/CO=3, WHSV=4.67-18.19 L/ g.h, P=10 bar, TOS = 50 h.

A similar trend was observed for the CH_4 selectivity (**Figure 3**). The methane selectivity (excluding carbon monoxide) was relatively high at low CO_2 conversion on all catalysts approaching 80% at zero conversion. An increase in the CO_2 conversion results in a drop in the methane selectivity and production of higher C_{2+} hydrocarbons. Similar behavior for methane selectivity was previously reported [66] in FT synthesis with syngas over promoted iron catalysts. Higher methane selectivity was observed over the $FeMo/ZrO_2$, $FeBi/ZrO_2$, $FeIn/ZrO_2$ and

FeSb/ZrO_2 samples (**Figure 3**). Addition of potassium with the second promoter results in a decrease in the methane selectivity over all promoted iron catalysts.

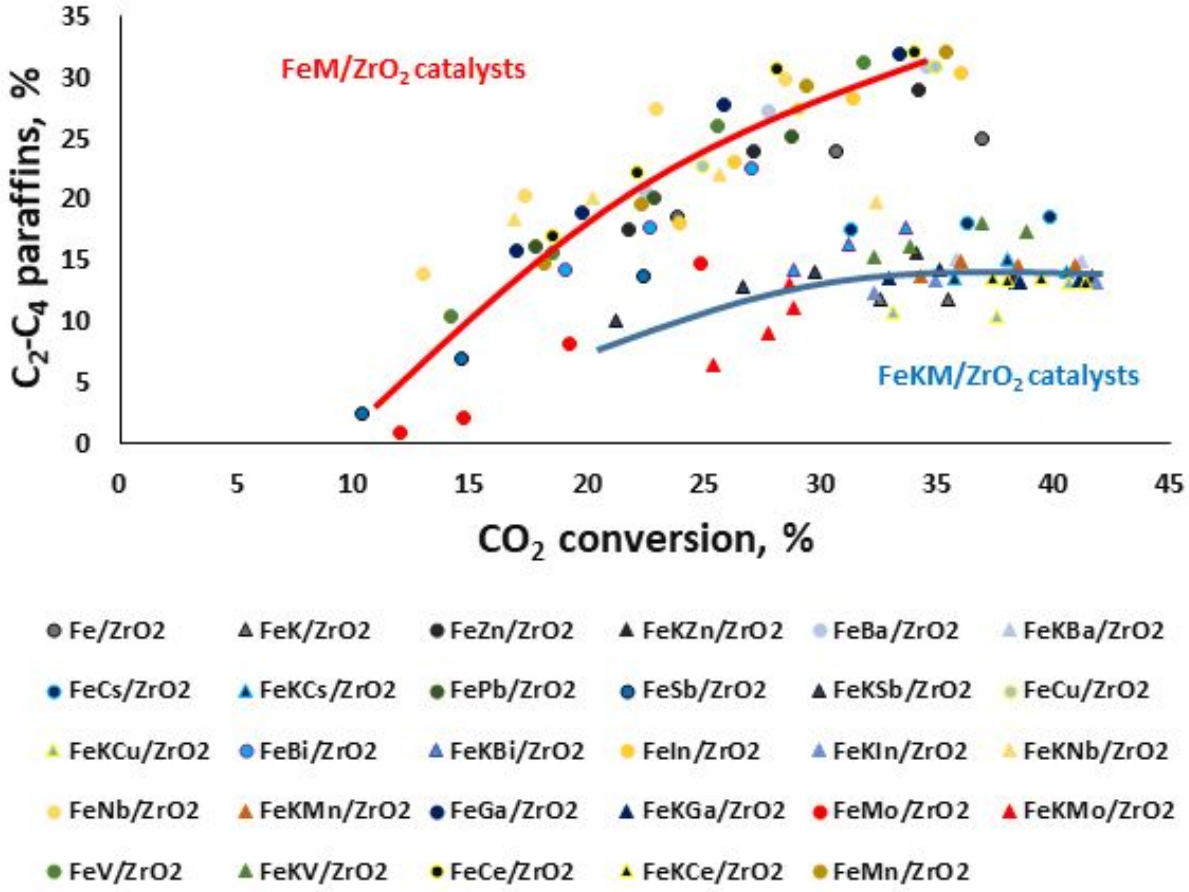

Figure 5. C_2-C_4 paraffins selectivity versus carbon dioxide conversion for Fe/ZrO_2 promoted catalysts. T=350°C, H_2/CO=3, WHSV=4.67-18.19 L/ g.h, P=10 bar, TOS = 50 h.

The light olefin selectivity data are displayed in **Figure 4**. Dependence of light olefin selectivity (**Figure 4**) on the CO_2 conversion shows two different behaviors. The first trend is observed for the promoted iron catalysts, which do not contain alkaline metals (potassium or cesium). The light olefin selectivity varies between 5 and 15% and is not, to any noticeable extent, affected by the CO_2 conversion level. The second trend is seen for the promoted iron catalysts containing potassium or cesium. The alkaline containing catalysts show higher light olefin

selectivities. The light olefin selectivity shows some decrease, when the CO_2 conversion increases. **Figure 4** has allowed identification of the most efficient promoters for iron catalysts. Clearly, the presence of potassium is essential to obtain higher light olefin selectivity. In addition to potassium, Mo, Cu, Cs, Ce and Ga seem to be efficient promoters, further increasing the selectivity of CO_2 hydrogenation to light olefins. The phenomenon is more pronounced for the FeKMo/ZrO_2 catalyst.

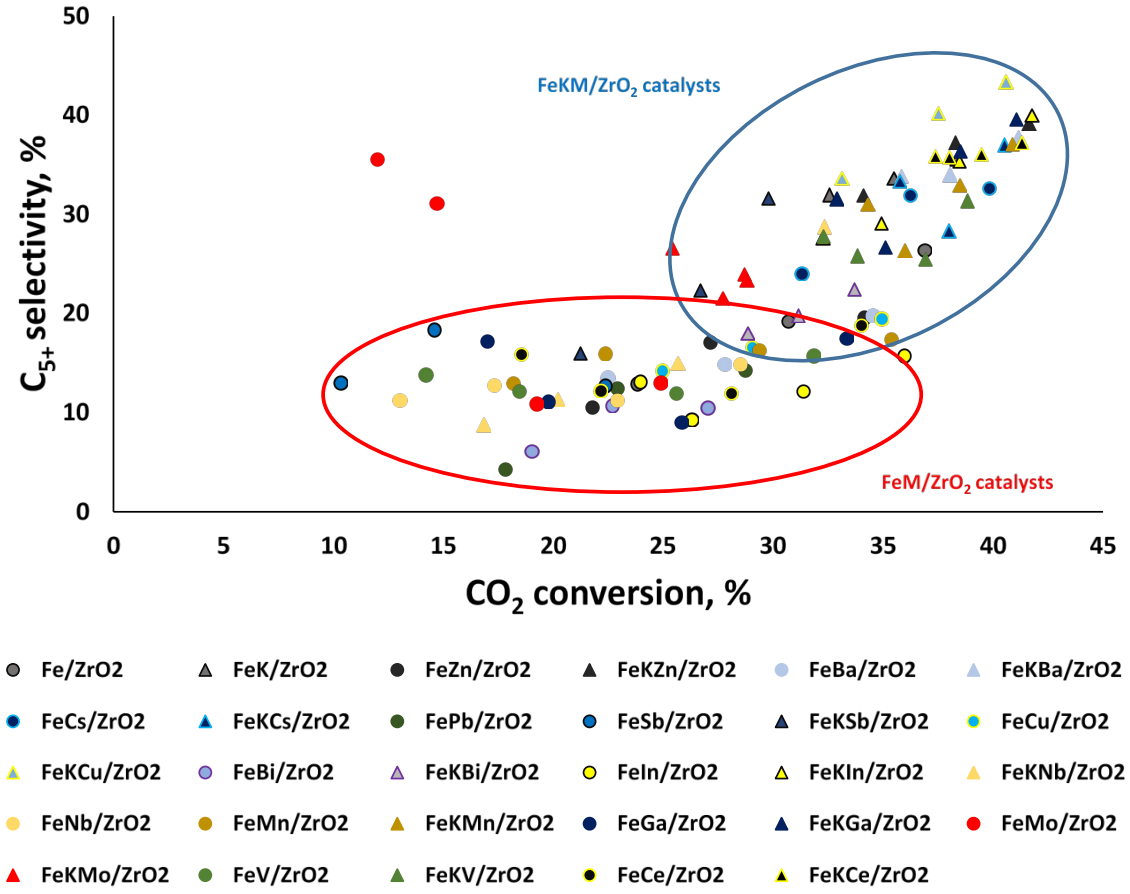

Figure 6. C_{5+} selectivity versus carbon dioxide conversion for Fe/ZrO_2 promoted catalysts. T=350°C, H_2/CO=3, WHSV=4.67-18.19 L/ g.h, P=10 bar, TOS = 50 h.

Table 1. Properties of selected supported Fe catalysts.

Sample	Fe content[a] (wt%)	K content[a] (wt%)	Promoter content[a] (wt%)	Total H_2 consum[b] (mmol/g)	S_{BET}[c] (m^2/g)	V_{tot}[d] (cm^3/g)	CO_2 ads. from TPD (μmol/g)	TOF, s^{-1}
ZrO_2	-	-	-	-	95.6	0.286	197.5	-
Fe/ZrO_2	10.09	-	-	1.81	70.0	0.212	46.9	0.13
FeK/ZrO_2	10.35	1.51	-	2.01	57.6	0.171	388.2	0.26
$FeKCs/ZrO_2$	9.66	1.11	1.05	2.45	58.4	0.173	474.4	-
$FeKCu/ZrO_2$	10.22	1.56	0.77	2.16	66.8	0.200	342.0	-
$FeKGa/ZrO_2$	10.38	1.46	0.33	2.62	47.6	0.174	312.9	0.50
$FeKMo/ZrO_2$	10.36	1.53	2.87	2.86	64.3	0.185	102.3	0.15
$FeKCe/ZrO_2$	11.01	1.47	0.97	2.70	65.4	0.176	246.0	-

[a]Fe and promoter content from XRF.
[b]The total H_2 consumption from TPR analysis.
[c]BET surface area.
[d]Single point desorption total pore volume of pores, P/P_0=0.975
[e]TOF was calculated[69] from average size of iron carbide nanoparticles in the activated catalysts using the density of Hägg iron carbide Fe_5C_2 (ρ = 7.57 g/cm^3) and assuming 14 Fe atoms/nm^2.

Let us now consider variation of light paraffin and C_{5+} hydrocarbon selectivities with the CO_2 conversion over the promoted iron catalysts. The FeM/ZrO_2 catalysts, which do not contain alkaline metals, show a noticeable increase in the C_2-C_4 paraffin selectivity with the CO_2 conversion (**Figure 5**). The light paraffin selectivity increases from 0 to 35%, as the CO_2 conversion rises from 10 to 40%. This suggests that on the one hand, the C_2-C_4 paraffins seem to

be secondary products over iron catalysts. They probably originate from hydrogenation of light olefins or C_nH_m surface species, which can be common precursors of both light olefins or paraffins. On the other hand, the FeKM/ZrO_2 catalysts, i.e., with potassium, present a much smaller variation of the C_2-C_4 paraffin selectivity with the CO_2 conversion (**Figure 5**). This suggests that secondary hydrogenation of light olefins or common surface precursors would be less significant in the presence of alkaline promoters. Instead, over the latter catalysts, higher CO_2 conversion results in the increase in the selectivity to the C_{5+} hydrocarbons (**Figure 6**). Finally, in contrast to FeKM/ZrO_2, over the FeM/ZrO_2 catalysts, the C_{5+} selectivity seems to be less dependent on the CO_2 conversion, which varies between 5 and 20%.

The catalyst stability is another important characteristic of CO_2 hydrogenation to light olefins. The stability was further tested in a fixed bed reactor. The catalyst results obtained with the laboratory fixed bed reactor show similar trends compared to the results measured in the HTE tests. **Figure S1, Supporting Information (SI)** shows the CO_2 conversion as a function of time-on-stream during 48 h of reaction. It is clear that the Fe/ZrO_2 reference catalyst deactivates with the reaction time, the CO_2 conversion drops from 20 to 8%. All the studied promoted catalysts showed higher activity than the reference catalyst (up to 7 times higher). In the case of the catalysts promoted only with K, the activity increases up to 4 times compared to the reference Fe/ZrO_2 catalyst, while the addition of a second promoter can further enhance the activity compared to the catalysts promoted solely with an alkaline metal. Note that not only the activity but also the stability was also enhanced in the presence of these promoters. The light olefin selectivity did not significantly change during the reaction with the exception of FeKMo/ZrO_2, which shows a steady increase in the light olefin selectivity with the reaction time.

In order to provide further insights into the enhancement of the catalytic performance on the promotion, the Fe/ZrO_2 (reference), FeK/ZrO_2, FeKMo/ZrO_2, FeKCu/ZrO_2, FeKCs/ZrO_2,

FeKCe/ZrO_2 and FeKGa/ZrO_2 catalysts have been investigated by a combination of characterization techniques.

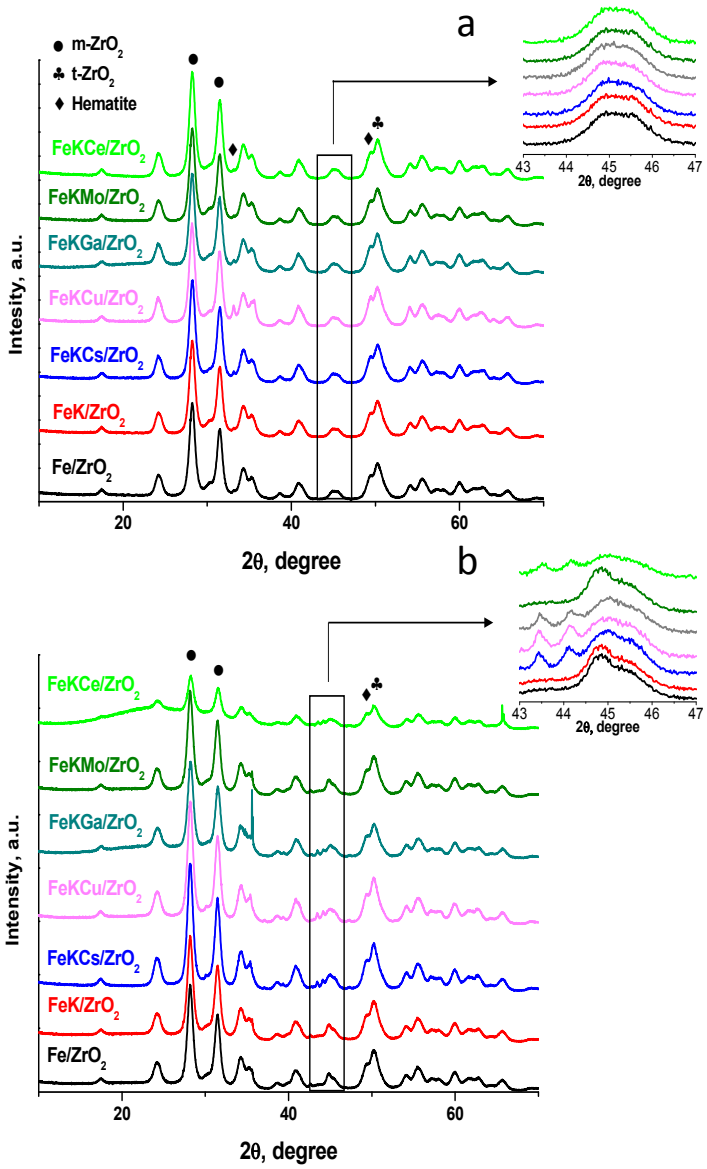

Figure 7. XRD patterns of the catalysts after calcination (a) and after reaction (b).

3.2 Catalyst characterization

The XRF elemental analysis data for selected promoted iron catalysts are displayed in **Table 1**. All the catalysts have similar iron contents close to nominal value (around 10 wt. %). At the same

time, the potassium content was slightly higher than expected (around 1.5 wt. %), while the amount of Cs, Ce, Cu, and Ga was as expected, 50:1 in molar ratio relative to iron. Only the Mo promoted catalyst shows a higher Fe/Mo ratio. The calcined catalysts display the characteristic XRD peaks (**Figure 7a**) attributed to the zirconia support[70,71]. The XRD peaks located at 28.2 and 31.5° are assigned to monoclinic zirconia (JCPDS 37-1484), while the peak at 50.3° reveals the presence of tetragonal zirconia (JCPDS 17-0923). Even though some broad hematite (Fe_2O_3, JCPDS13-0534) peaks were detected, the intensity of them was rather low. Significant broadening of these peaks indicates small size of iron oxide nanoparticles (below 5 nm). No diffraction peaks assignable to the crystalline phases of promoters were observed. This was is attributed to their low content in the catalysts.

We also performed XRD measurements (**Figure 7b**) for reference and promoted catalysts after conducting the CO_2 hydrogenation reaction. The spent FeKCs/ZrO_2, FeKCu/ZrO_2, FeKGa/ZrO_2, and FeKGa/ZrO_2 catalysts exhibit diffraction peaks at 2θ angle of 43.4 and 44.1° that can be attributed to the iron carbide phases such as Hägg iron carbide (Fe_5C_2, JCPDS20-0509) formed during the reaction. Because of similarity of XRD patterns attributed to different iron carbide, identification of individual iron carbide phases by means of XRD analysis is challenging.

Figure 8 shows the CO_2 TPD curves for promoted iron catalysts, the amount of CO_2 adsorbed over the catalysts is shown in **Table 1** and **Table S1, SI**. The profiles exhibit three peaks: the first one located at 80-100°C, corresponding to weak basic sites, the second one at 150-200°C assigned to medium basic sites and the third one at 350 °C attributed to strong basic sites. The deconvolution of the CO_2-TPD profiles is illustrated by **Figure S2, SI**. ZrO_2 is a basic oxide and the TPD profile of pure zirconia is similar to that previously reported in the literature [72,73]. The deconvolution (**Figure S2, SI**) displays two broad CO_2 TPD peaks at 100°C and 220°C. This suggests the presence of a wide range of relatively weak and medium basic sites. Addition of iron to ZrO_2 reduces the

CO_2-TPD peak intensity. It seems that some medium basic sites of zirconia are neutralized by interaction with the added iron oxides. The promotion with potassium and cesium leads to an increase in the number of adsorbed CO_2 and results in two distinct peaks, the first at 120°C corresponding to the weak basicity and the second at 300-420°C corresponding to stronger basicity. The intensity of these peaks correlates with the amount of alkaline metals in the catalysts. Addition of the second promoter (except for Cs) results in a decreasing concentration of basic sites, indicating some interaction of the promoter with potassium and zirconia. Such a lower concentration of basic sites has been observed in the iron catalyst simultaneously promoted with potassium and molybdenum (**Figure 8**).

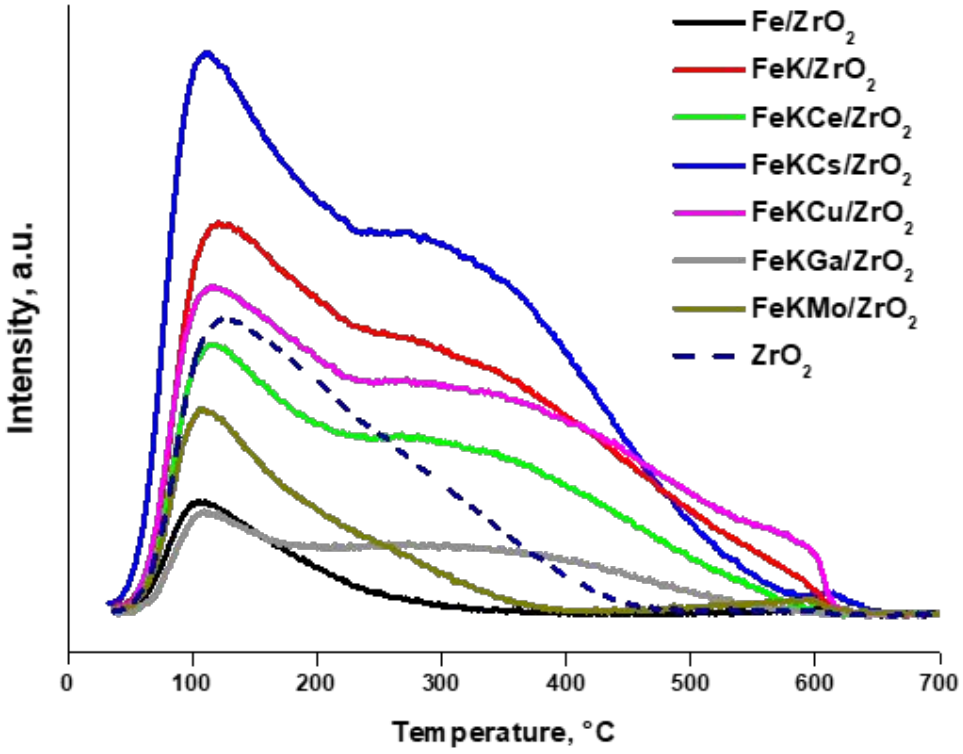

Figure 8. CO_2 TPD profiles adsorbed over ZrO_2 and iron catalysts.

The TPR profiles of the reference Fe/ZrO_2, FeK/ZrO_2, $FeKCs/ZrO_2$, $FeKCe/ZrO_2$ and $FeKGa/ZrO_2$ catalysts are displayed in **Figure 9.** The amount of hydrogen consumed for catalyst reduction is given in **Table 1.** The first reduction peak at ~380 °C can be attributed to the hematite reduction to magnetite, $Fe_2O_3 \rightarrow Fe_3O_4$,[74] and the second broader peak related to the successive reduction of iron oxides, $Fe_3O_4 \rightarrow FeO \rightarrow Fe$. [75–77] This second peak is centered at ~500 °C for the reference Fe/ZrO_2 and FeK/ZrO_2 catalysts.

For the $FeKCs/ZrO_2$, $FeKCe/ZrO_2$ and $FeKGa/ZrO_2$ catalysts, this peak shifts toward higher temperatures. Addition of Cs, Ga, Ce seems to give place to a strong interaction of iron oxide with the promoters[78] and hinders reduction of the magnetite phase. Note that these promoters do not affect the first reduction step (Fe_2O_3 to Fe_3O_4). On the other hand, the H_2-TPR profile of $FeKMo/ZrO_2$ shows a shift to higher temperatures for both peaks.

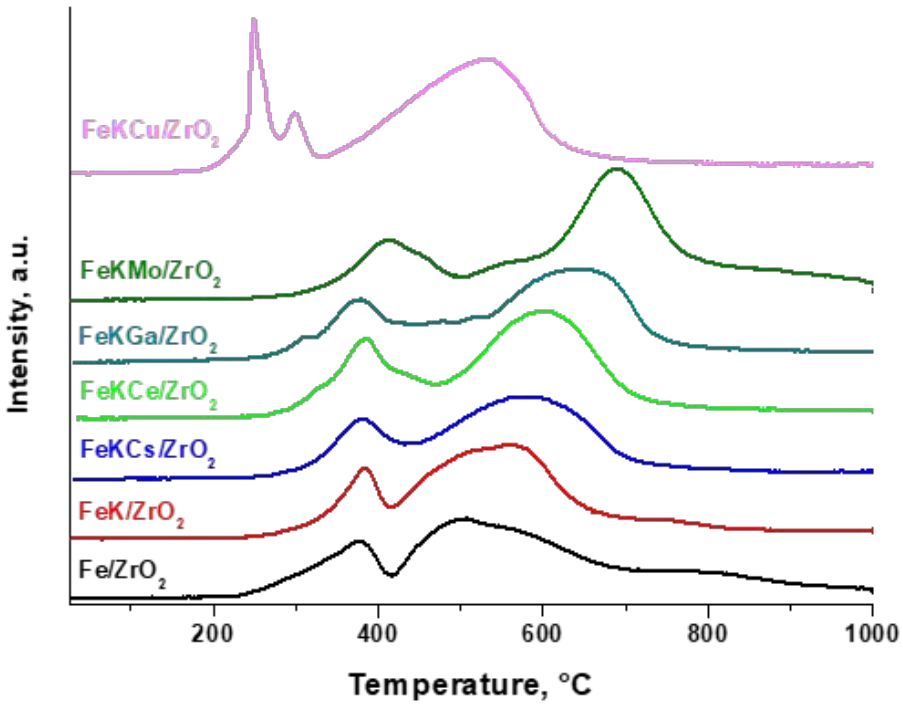

Figure 9. H_2-TPR profiles of reference catalysts and catalysts promoted with K, Cs, Ce, Ga, Mo, and Cu.

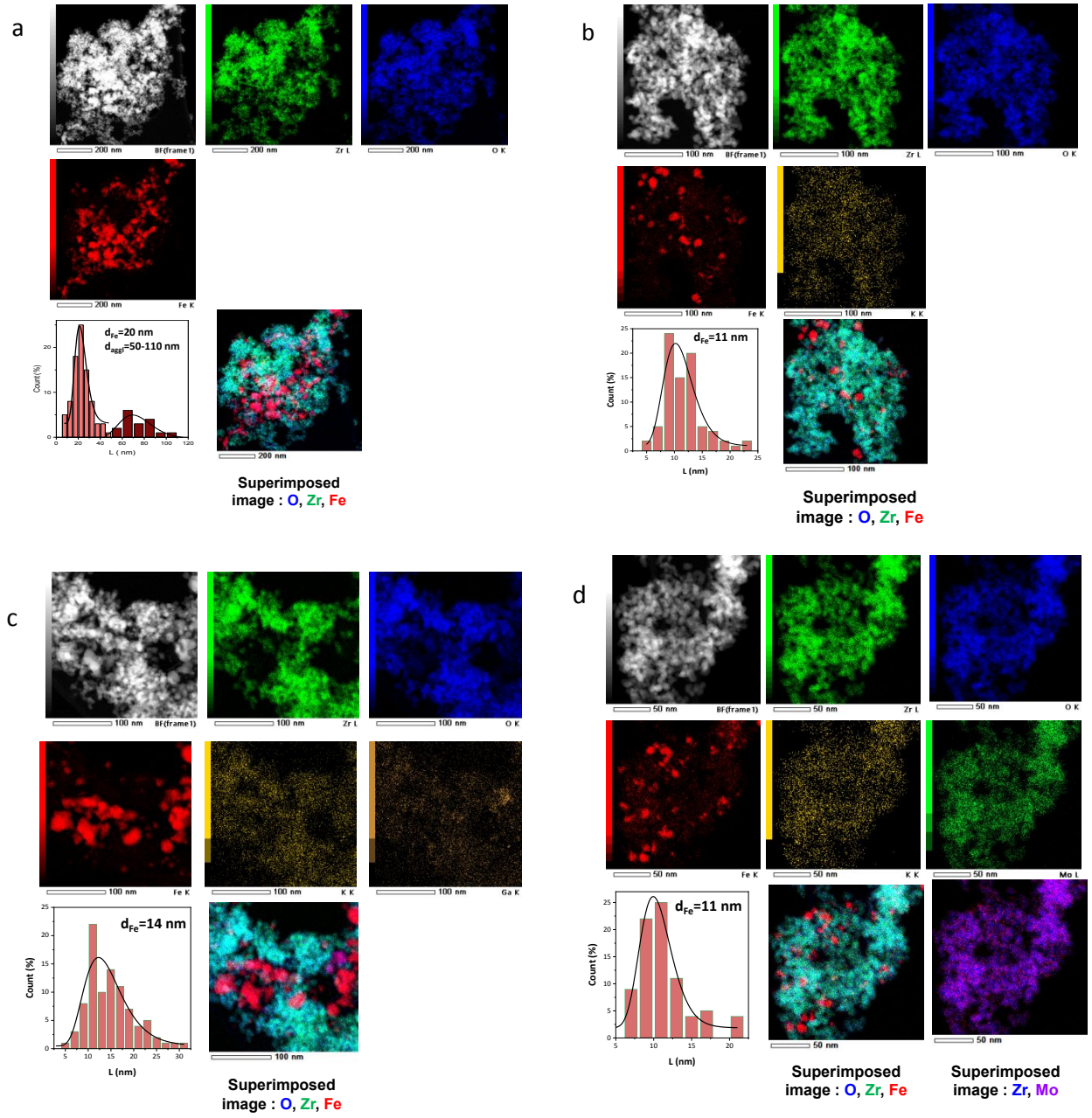

Figure 10. STEM-HAADF, SEM-EDX mapping and histograms of iron nanoparticle sizes for the activated Fe/ZrO_2 (a), FeK/ZrO_2 (b), $FeKGa/ZrO_2$ (c) and $FeKMo/ZrO_2$ (d) catalysts.

So, the molybdenum presence clearly affects the different iron oxide reduction steps. Finally, the H_2-TPR profile of $FeKCu/ZrO_2$ displays two reduction peaks at ~250 and 298 °C, which shift to lower temperatures compared to the reference Fe/ZrO_2 sample, in agreement with the literature [74]. The intensity of peak at 250°C can also contribute from the reduction of copper [79]. Indeed, the

presence of copper in the catalyst may facilitate iron oxide reduction. Remarkably, addition of promoters results in a higher amount of consumed hydrogen (**Table 1**). It seems that the promotion slows down interaction of iron with zirconia and increases the amount of reducible iron. Note that the amounts of incorporated promoters compared to iron are rather small to significantly contribute to the intensity of TPR peaks.

The information about dispersion of iron and localization of promoters was extracted from the STEM-HAADF and STEM- EDS analyses of activated iron catalysts. The high-resolution STEM images of the reference Fe/ZrO_2 catalyst, FeK/ZrO_2, $FeKGa/ZrO_2$ and $FeKMo/ZrO_2$ are shown in **Figure S3, SI.** The catalysts show agglomerated nanoparticles with mainly oval shape and narrow size distribution from 6 to 27 nm. The average catalyst particle size was around 14 nm for all studied catalysts**.** No clear signature of Ga and K was observed in the images, because of their small amounts and their Z number relatively close to the one of Fe and Zr. At the same time, because of noticeable Z-contrast in STEM-HAADF mode, atoms and atomic clusters of Mo are visible as light spots and agglomerates in $FeKMo/ZrO_2$ (**Figure S4, SI**).

The STEM-HAADF and STEM-EDS images have provided further information about iron particle sizes and promoter localization in the supported catalysts (**Figure 10**). The histograms of iron nanoparticle sizes were estimated from the STEM-EDS Fe elemental maps. In the reference Fe/ZrO_2 sample, iron nanoparticles of 20 nm mean diameter were homogeneously dispersed in the ZrO_2 matrix. Local agglomeration of iron nanoparticles was also observed. This is most probably due to the fact that TEM acquire a projection of the volume and therefore, the superposition of nanoparticles in the projection within the analyzed volume leads to a certain agglomeration of nanoparticles. Interestingly, relatively low concentration of oxygen was found in the iron-rich areas compared to the iron-poor ones (**Figure S5, SM**). This could be indicative of lower fraction of iron oxides and higher extent of iron carbidization in the activated catalysts. Since the specimens were

deposited onto carbon supports and the analyses were carried out for long time, it is difficult to estimate the carbon content in the samples. This is due to the superposition of the carbon signal from the membrane and occurrence of carbon contamination during the long duration scanning. The promoted FeK/ZrO_2, $FeKGa/ZrO_2$ and $FeKMo/ZrO_2$ catalysts exhibited much smaller iron nanoparticles of 11-14 nm homogeneously dispersed within the ZrO_2 matrix, without any Fe nanoparticles agglomeration (**Figure 10**). The promoters (K, Ga and Mo) appear to be homogeneously distributed in very small amounts. EDS also confirmed nearly atomic Mo distribution over zirconia (**Figures S4, SI**).

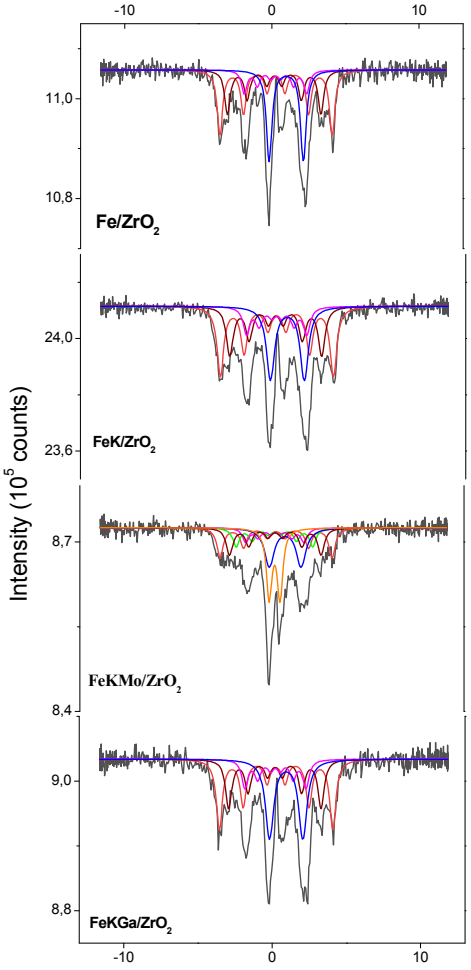

Figure 11. Mössbauer spectra after activation measured at -153 °C.

In order to get a deeper understanding of the catalytic performance, the reference and promoted iron catalysts were characterized using *in-situ* Mössbauer spectrometry under the flow of CO and reaction mixture ($CO_2 + H_2$). After the CO activation at 350 °C (**Figure 11**), iron Hägg carbide and wüstite (FeO) were observed in all samples. The promotion of Fe/ZrO_2 catalyst with K and Mo results in a higher fraction of iron carbide (**Table 2**). A noticeable concentration of metastable (ϵ'-$Fe_{2.2}C$) carbide [63] was observed in the $FeKMo/ZrO_2$ catalyst after the activation.

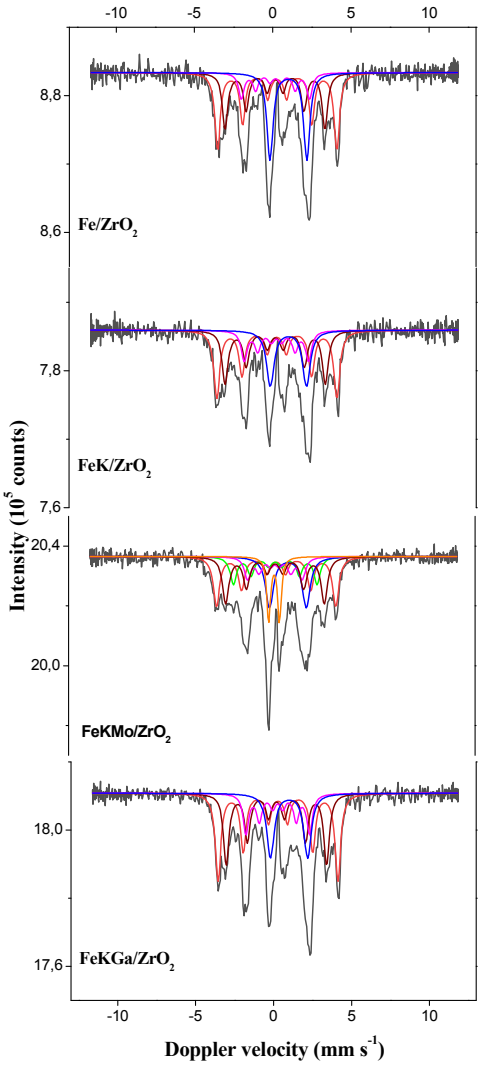

Figure 12. Mössbauer spectra after reaction measured at -153 °C.

Figure 12 shows the *in-situ* Mössbauer spectra after catalyst exposure to the reaction conditions (H_2/CO_2 = 3, 350 °C and 10 bar). Two types of Mössbauer spectra modification were observed. On the one hand, there is a slight improvement in the crystallinity of the Hägg iron carbide species. In the Mössbauer spectroscopy, the crystallinity was reflected by the linewidth of measured signal. The reference Fe/ZrO_2 catalyst after the 24 h of reaction exhibits better defined Hägg structures. The linewidth of Mössbauer signals decreased from 0.45 to 0.42 mm/s (**Table 2**).

The same tendency was observed for all promoted catalysts. On the other hand, the fraction of iron carbide seems to further increase after conducting the CO_2 hydrogenation. This is shown by the lower amount of unreduced wüstite species in the spent catalysts compared to that in the counterparts activated in CO. In contrast to other catalysts, $FeKGa/ZrO_2$ after reaction did not show any increase in the iron carbide content, indicating a smaller effect of Ga addition on iron carbidisation. Only the slightly smaller linewidth values indicate the presence of better defined Hägg carbide species in $FeKGa/ZrO_2$ compared to FeK/ZrO_2. Note that the $FeKMo/ZrO_2$ catalyst showed the higher fraction of iron carbide among all studied promoted iron catalysts after conducting CO_2 hydrogenation.

Carbon deposition could be a limitation of CO_2 hydrogenation resulting in a loss of catalytic activity. **Figure S6, SI** shows the thermogravimetric analysis (TGA) data for the spent ZrO_2-supported catalysts. The first small loss around 150 °C is normally generated by the water elimination and possible dehydration of iron oxyhydroxide (FeOOH).[60] Above 300 °C, significant weight losses produced by the combustion of carbon deposits and carbides can be observed. Interestingly, the reference catalyst presents a smaller weight loss. So, the enhancement of stability observed during the CO_2 hydrogenation reaction over the promoted catalysts (**Figure S1, SI**) seems not to be related to the catalyst ability to avoid carbon deposition and can possibly be assigned to

other phenomena. One possible reason for the better stability of the catalysts could be related to less sintering of the iron carbide nanoparticles after the addition of the promoters.

Table 2. Mössbauer fitted parameters of the ZrO_2-based catalysts, obtained at -153 °C.

Sample/ Treatment	*IS (mm·s^{-1})*	*QS (mm·s^{-1})*	*Hyperfine field (T)*	*Γ (mm·s^{-1})*	*Phase*	*Spectral contribution (%)*
Fe/ZrO_2 CO, 350 C	0.28	-	23.7	0.45	χ-Fe_5C_2 (I)	36
	0.16	-	19.7	0.45	χ-Fe_5C_2 (II)	25
	0.24	-	13.2	0.45	χ-Fe_5C_2 (III)	13
	0.98	2.32	-	0.45	$Fe_{1-x}O$ (SPM[a])	26
Fe/ZrO_2 H_2/CO_2=3 350 C, 10 bar	0.28	-	23.7	0.42	χ-Fe_5C_2 (I)	37
	0.15	-	19.8	0.42	χ-Fe_5C_2 (II)	27
	0.17	-	13.6	0.42	χ-Fe_5C_2 (III)	12
	1.00	2.35	-	0.47	$Fe_{1-x}O$ (SPM)	24
FeK/ZrO_2 CO, 350 C	0.26	-	23.7	0.54	χ-Fe_5C_2 (I)	37
	0.18	-	19.3	0.54	χ-Fe_5C_2 (II)	26
	0.24	-	12.6	0.54	χ-Fe_5C_2 (III)	14
	0.96	2.28	-	0.65	$Fe_{1-x}O$ (SPM)	23
FeK/ZrO_2 H_2/CO_2=3 350 C, 10 bar	0.27	-	23.8	0.47	χ-Fe_5C_2 (I)	36
	0.17	-	19.9	0.47	χ-Fe_5C_2 (II)	29
	0.24	-	12.8	0.47	χ-Fe_5C_2 (III)	16
	1.00	2.31	-	0.58	$Fe_{1-x}O$ (SPM)	19
$FeKMo/ZrO_2$ CO, 350 C	0.28	-	23.5	0.53	χ-Fe_5C_2 (I)	20
	0.23	-	19.2	0.53	χ-Fe_5C_2 (II)	18
	0.20	-	11.2	0.53	χ-Fe_5C_2 (III)	10
	0.17	-	16.1	0.53	ϵ'-$Fe_{2.2}C$	13
	0.17	0.74	-	0.45	Fe_xC (SPM)	20
	0.90	2.15	-	0.77	$Fe_{1-x}O$ (SPM)	19
$FeKMo/ZrO_2$ H_2/CO_2=3 350 C, 10 bar	0.27	-	23.7	0.49	χ-Fe_5C_2 (I)	25
	0.21	-	19.6	0.49	χ-Fe_5C_2 (II)	24
	0.20	-	10.9	0.49	χ-Fe_5C_2 (III)	11
	0.22	-	16.6	0.49	ϵ'-$Fe_{2.2}C$	14
	0.14	0.70	-	0.28	Fe_xC (SPM)	10
	1.02	2.35	-	0.61	$Fe_{1-x}O$ (SPM)	16
$FeKGa/ZrO_2$ CO, 350 C	0.26	-	23.8	0.50	χ-Fe_5C_2 (I)	35
	0.19	-	19.3	0.50	χ-Fe_5C_2 (II)	24
	0.22	-	12.3	0.50	χ-Fe_5C_2 (III)	14
	0.95	2.24	-	0.67	$Fe_{1-x}O$ (SPM)	27
$FeKGa/ZrO_2$ H_2/CO_2=3 350 C, 10 bar	0.28	-	23.9	0.43	χ-Fe_5C_2 (I)	36
	0.19	-	20.0	0.43	χ-Fe_5C_2 (II)	29
	0.26	-	12.7	0.43	χ-Fe_5C_2 (III)	17
	0.99	2.38	-	0.57	$Fe_{1-x}O$ (SPM)	18

Experimental uncertainties: Isomer shift: I.S. ± 0.02 mm s^{-1}; Quadrupole splitting: Q.S. ± 0.02 mm s^{-1}; Line width: Γ ± 0.03 mm s^{-1}; Hyperfine field: ± 0.1 T; Spectral contribution: ± 3%; [a]Very small, superparamagnetic (SPM)

4. Discussion

CO_2-FT synthesis occurs at 300-350°C and is focused on the production of light olefins. Compared to the "methanol-mediated" processes occurring over metal-oxide/zeolite catalysts, CO_2-FT synthesis exhibits higher yields of olefins and lower selectivity to CO [31,32]. Iron catalysts are the catalysts of choice for light olefin synthesis from CO_2 via the FT route. The selection of efficient promoters for iron catalysts seems to be the key for the selectivity control of this reaction. Alkaline metals [34,37–46], copper [52,53], manganese [45,46,54], zinc [31,44,55,56] and cobalt [47–51] have been the most investigated promoters for iron CO_2-FT catalysts. At the same time, very limited attention has been paid to the promotion of iron CO_2-FT catalysts with other elements. In this work, HTE combined with catalyst characterization have allowed identification of new efficient promoters and also provided important information about the influence of these promoters on different reaction elementary steps.

CO_2-FT synthesis is a complex multi-stage reaction [23,24,42,80]. It can be therefore suggested that different reaction stages can be affected to a different extent by the promotion. The experimental results shown in **Figures 2-6** illustrate the effects of added promoters on different reactions steps. **Figure 2** shows the CO selectivity close to 100% at the CO_2 conversion approaching zero. CO seems indeed, to be the primary product of CO_2 hydrogenation over iron catalysts. Important, the experimental results obtained for numerous promoted iron catalysts exhibit a similar trend. RWGS is a fast reaction and is readily catalyzed by iron oxides (e. g. Fe_3O_4) [31,42]. The presence of noticeable concentrations of iron oxide species in the working catalysts has been identified by Mössbauer spectrometry. This explains similar behavior of all promoted catalysts in RWGS. Interestingly, almost all promoted catalysts showed much higher CO selectivity at the same CO_2 conversion compared to the reference Fe/ZrO_2 catalyst. The added promoters could therefore

contribute to RWGS. This also coincides with higher overall activity (FTY) of the promoted catalysts compared to the reference one (**Figure 1**).

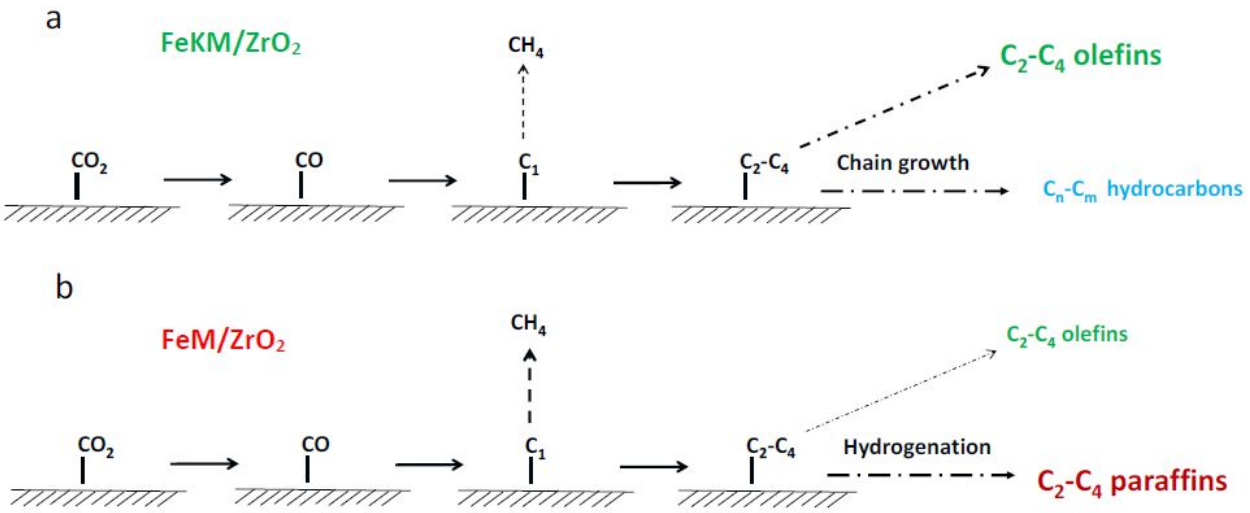

Figure 13. Reaction paths in CO_2 hydrogenation over promoted iron catalysts with (a) and without (b) potassium.

The methane selectivity versus conversion curve (**Figure 3**) also agrees with the suggested reaction sequence (**Figure 13**). Higher methane selectivity is observed at lower CO_2 conversion, then the methane selectivity drops at higher conversion. At low conversion, hydrogenation of C_1 monomer seems to prevail over its oligomerization. At higher CO_2 conversion and higher surface concentration of C_1 monomers, their oligomerization becomes more favorable and leads to adsorbed C_2-C_4 species. This trend has been seen for all catalysts, with somewhat lower methane selectivity at the same conversions observed for $FeMo/ZrO_2$, $FeKMo/ZrO_2$ and $FeKSb/ZrO_2$.

Very different correlations between light olefin selectivity and conversion have been observed for the catalysts with and without alkaline metals (**Figure 4**). The light olefin selectivity over FeM/ZrO_2 (without alkaline metals) was much lower compared to the $FeKM/ZrO_2$ catalysts promoted with potassium and it does not noticeably vary as a function of CO_2 conversion. The

higher selectivity to light olefins over the FeKM/ZrO_2 catalysts decreases as a function of CO_2 conversion. For the catalysts without alkaline promoters, increased CO_2 conversion results in higher selectivity to C_2-C_4 hydrocarbons, while for the catalysts containing alkaline metals, higher selectivity to the C_{5+} hydrocarbons was measured at higher CO_2 conversions. Higher conversion leads therefore to a higher selectivity to the C_{5+} hydrocarbons, which can be attributed to enhanced surface oligomerization of C_1 monomeric species and readsorption of light olefins [81,82], which may reinitialize oligomerization on iron catalysis, both phenomena favoring production of longer chain hydrocarbons.

The possible reaction paths of CO_2-FT synthesis over iron catalysts have been summarized in **Figure 13.** The first step in CO_2-FT synthesis over iron catalysts is CO_2 hydrogenation to CO followed by formation of C_1 adsorbed monomers. Then, the adsorbed C_1 monomers can be either hydrogenated to yield methane or to undergo oligomerization to different C_n adsorbed species. Desorption of C_2-C_4 adsorbed species should produce light olefins (ethylene, propylene or butylene), while their hydrogenation leads to light paraffins, the latter also possibly be produced via olefin re-adsorption (and subsequent hydrogenation) [83–85]. Further reactions of adsorbed C_2-C_4 species with C_1 monomer produce longer-chain hydrocarbons.

The rates of hydrogenation of adsorbed C_2-C_4 species and rates of oligomerization seem to be different over the catalysts with (**Figure 13a**) and without potassium (**Figure 13b**). These phenomena also explain the role of alkaline promoters. The promotion with alkaline metals results in a decrease in the catalyst hydrogenation ability and at the same time, increases the rate of oligomerization of C_1 surface monomers. Thus, over the catalysts containing alkaline metals, the oligomerization limits the light olefin selectivity, while the contribution of hydrogenation of adsorbed C_2-C_4 species or secondary hydrogenation of light olefins is not significant. This suggests that, in order to boost the light olefin selectivity over the catalysts promoted with alkaline metals,

the surface oligomerization should be hindered after the formation of the C_4 surface fragments. Similar effects were previously observed in the CO hydrogenation over iron catalysts [66]. The second promoter should therefore, slow down chain growth in particular for C_{5+} hydrocarbon fragments, without any major enhancement of hydrogenation.

The key issue in the catalyst design for CO_2-FT synthesis is therefore light olefin selectivity. **Figure 4** shows the light olefin selectivity versus conversion, and it enables identification of the most efficient second promoters such as Mo, Cs, Ga, Ce and Cu. Note that in order to reach higher selectivity to light olefins, these promoters should be used in combination with potassium.

The catalyst promoters are usually divided into two types: structural promoters, which might generate an enhanced iron dispersion and carbidization and give better mechanical resistance and electronic promoters, which could enhance the intrinsic activity of active sites (TOF). Several phenomena can be responsible for the observed increase in the light olefin selectivity over the catalysts promoted simultaneously with potassium and other elements. First, the STEM-HAADF and STEM-EDS observations of the promoted catalysts (**Figure 10**) showed noticeable increase in the iron dispersion in the activated catalysts compared to the reference Fe/ZrO_2 counterpart. Consequently, higher iron dispersion can contribute to the increase in FT reaction rate and light olefin selectivity. Second, the addition of promoters can modify the extent of iron carbidization and reduction. The *in-situ* Mössbauer data (**Table 2**) show that the presence of the promoters such as Mo, K and Ga results in a higher fraction of iron carbide. For the $FeKMo/ZrO_2$ catalyst promoted with potassium and molybdenum, the increase in iron carbidization during the reaction coincides with the continuous increase in light olefin selectivity. The TPR results (**Figure 9**) show easier iron reduction in the copper-promoted catalysts. Third, the promotion enhances the RWGS reaction, which is an important step in CO_2-FT synthesis and often affects the overall activity. Indeed, most of the promoted catalysts showed higher CO selectivity at a given CO_2

conversion compared to reference Fe/ZrO_2. Four, the promotion affects the catalyst basicity and, hence, adsorption of CO_2, which is an acid molecule. The promotion with potassium principally results in the buildup of strong basic sites (**Figure 8, Figure S2** and **Table S1, SI**). Note that extremely strong or weak basicity does not seem to be optimal for obtaining high concentrations of reactive CO_2 adsorbed molecules. Addition of the second promoter mediates the basicity of FeK/ZrO_2 catalysts (**Table S1, SM**) and thus, favors the CO_2 activation. Five, TOF calculated from the iron carbide particle size (**Table 1**) measured by TEM images shows 2–4 times higher values in the presence of K and K-Ga-promoters, while there is a slightly effect on TOF when Mo is added simultaneously with K.

5. Conclusion

HTE tests allowed the identification of new suitable promoters and structure-performance-correlations over zirconia supported iron catalysts for CO_2 hydrogenation to light olefins. The presence of alkaline promoters seems to be indispensable for the selectivity enhancement towards light olefins over iron catalysts. Complementary to potassium, the promotion of ZrO_2-supported catalysts with Cs, Mo, Cu, Ga, and Ce resulted in further increase in the light olefin selectivity. Better iron dispersion, higher extent of iron carbidization and optimized basicity coincide with the enhanced light olefin selectivity in the promoted catalysts. The catalyst basicity required for CO_2 adsorption is enhanced by the promotion with alkaline metals and mediated by the second promoter.

CO_2-FT synthesis proceeds *via* intermediate production of carbon monoxide. The dependence of light olefin selectivity on the CO_2 conversion exhibits two different trends, depending on potassium promotion. Without potassium as promoter, the relatively low selectivity to light olefins is practically independent of the CO_2 conversion. The second trend is identified for

the iron catalysts containing simultaneously alkaline and second promoter. Over those catalysts much higher selectivity to light olefins shows a noticeable decrease with the increase in CO_2 conversion. Over the catalysts without alkaline metals, higher CO_2 conversion favors production of light paraffins, while the presence of potassium leads to higher selectivity towards longer chain hydrocarbons at higher conversion level. The second promoter, complementary to an alkaline metal, should hinder chain growth rates without any increase in the hydrogenation rate of surface intermediate species.

Acknowledgements

The authors acknowledge financial support from European Union (Interreg V project PSYCHE). The REALCAT platform is benefiting from a Governmental subvention administrated by the French National Research Agency (ANR) within the frame of the 'Future Investments' program (PIA), with contractual reference 'ANR-11-EQPX-0037'. GENESIS is supported by the Region Haute-Normandie, the Metropole Rouen Normandie, the CNRS via LABEX EMC and French National Research Agency as a part of the program "Future Investments" with the reference ANR-11-EQPX-0020.

Reference

(1) D'Alessandro, D. M.; Smit, B.; Long, J. R. Carbon Dioxide Capture: Prospects for New Materials. *Angew. Chemie - Int. Ed.* **2010**, *49* (35), 6058–6082. https://doi.org/10.1002/anie.201000431.

(2) Aresta, M.; Dibenedetto, A.; Angelini, A. Catalysis for the Valorization of Exhaust Carbon: From CO_2 to Chemicals, Materials, and Fuels. Technological Use of CO_2. *Chem. Rev.* **2014**, *114* (3), 1709–1742. https://doi.org/10.1021/cr4002758.

(3) Goeppert, A.; Czaun, M.; Jones, J. P.; Surya Prakash, G. K.; Olah, G. A. Recycling of Carbon Dioxide to Methanol and Derived Products-Closing the Loop. *Chem. Soc. Rev.* **2014**, *43* (23), 7995–8048. https://doi.org/10.1039/c4cs00122b.

(4) Ordomsky, V. V.; Dros, A.-B.; Schwiedernoch, R.; Khodakov, A. Y. Challenges and Role of Catalysis in CO_2 Conversion to Chemicals and Fuels. In *Nanotechnology in Catalysis*; Wiley-VCH Verlag GmbH & Co. KGaA: Weinheim, Germany, 2017; pp 803–850. https://doi.org/10.1002/9783527699827.ch30.

(5) Porosoff, M. D.; Yan, B.; Chen, J. G. Catalytic Reduction of CO_2 by H_2 for Synthesis of CO, Methanol and Hydrocarbons: Challenges and Opportunities. *Energy Environ. Sci.* **2016**, *9* (1), 62–73. https://doi.org/10.1039/c5ee02657a.

(6) Posada-Pérez, S.; Ramírez, P. J.; Evans, J.; Viñes, F.; Liu, P.; Illas, F.; Rodriguez, J. A. Highly Active Au/δ-MoC and Cu/δ-MoC Catalysts for the Conversion of CO_2: The Metal/C Ratio as a Key Factor Defining Activity, Selectivity, and Stability. *J. Am. Chem. Soc.* **2016**, *138* (26), 8269–8278. https://doi.org/10.1021/jacs.6b04529.

(7) Ye, R. P.; Ding, J.; Gong, W.; Argyle, M. D.; Zhong, Q.; Wang, Y.; Russell, C. K.; Xu, Z.;

Russell, A. G.; Li, Q.; Fan, M.; Yao, Y. G. CO_2 Hydrogenation to High-Value Products via Heterogeneous Catalysis. *Nat. Commun.* **2019**, *10* (1). https://doi.org/10.1038/s41467-019-13638-9.

(8) Navarro-Jaén, S.; Virginie, M.; Bonin, J.; Robert, M.; Wojcieszak, R.; Khodakov, A. Y. Highlights and Challenges in the Selective Reduction of Carbon Dioxide to Methanol. *Nat. Rev. Chem.* **2021**, *0123456789*. https://doi.org/10.1038/s41570-021-00289-y.

(9) Graciani, J.; Mudiyanselage, K.; Xu, F.; Baber, A. E.; Evans, J.; Senanayake, S. D.; Stacchiola, D. J.; Liu, P.; Hrbek, J.; Fernández Sanz, J.; Rodriguez, J. A. Highly Active Copper-Ceria and Copper-Ceria-Titania Catalysts for Methanol Synthesis from CO_2. *Science (80-.).* **2014**, *345* (6196), 546–550. https://doi.org/10.1126/science.1253057.

(10) Rodriguez, J. A.; Liu, P.; Stacchiola, D. J.; Senanayake, S. D.; White, M. G.; Chen, J. G. Hydrogenation of CO_2 to Methanol: Importance of Metal-Oxide and Metal-Carbide Interfaces in the Activation of CO_2. *ACS Catal.* **2015**, *5* (11), 6696–6706. https://doi.org/10.1021/acscatal.5b01755.

(11) Frusteri, F.; Cordaro, M.; Cannilla, C.; Bonura, G. Multifunctionality of Cu-ZnO-ZrO_2/H-ZSM5 Catalysts for the One-Step CO_2-to-DME Hydrogenation Reaction. *Appl. Catal. B Environ.* **2015**, *162*, 57–65. https://doi.org/10.1016/j.apcatb.2014.06.035.

(12) Bonura, G.; Cordaro, M.; Cannilla, C.; Mezzapica, A.; Spadaro, L.; Arena, F.; Frusteri, F. Catalytic Behaviour of a Bifunctional System for the One Step Synthesis of DME by CO_2 Hydrogenation. *Catal. Today* **2014**, *228*, 51–57. https://doi.org/10.1016/j.cattod.2013.11.017.

(13) Navarro-Jaén, S.; Virginie, M.; Morin, J.-C.; Thuriot, J. R.; Wojcieszak, R.; Khodakov, A.

Hybrid Monometallic and Bimetallic Copper-Palladium Zeolite Catalysts for Direct Synthesis of Dimethyl Ether from CO_2. *New J. Chem.* **2022**. https://doi.org/10.1039/D1NJ05734K.

(14) Navarro-Jaén, S.; Virginie, M.; Thuriot-Roukos, J.; Wojcieszak, R.; Khodakov, A. Y. Structure–Performance Correlations in the Hybrid Oxide-Supported Copper–Zinc SAPO-34 Catalysts for Direct Synthesis of Dimethyl Ether from CO_2. *J. Mater. Sci.* **2022**. https://doi.org/10.1007/s10853-022-06890-w.

(15) Mori, K.; Taga, T.; Yamashita, H. Isolated Single-Atomic Ru Catalyst Bound on a Layered Double Hydroxide for Hydrogenation of CO_2 to Formic Acid. *ACS Catal.* **2017**, *7* (5), 3147–3151. https://doi.org/10.1021/acscatal.7b00312.

(16) Xu, Z.; Mcnamara, N. D.; Neumann, G. T.; Schneider, W. F.; Hicks, J. C. Catalytic Hydrogenation of CO_2 to Formic Acid with Silica-Tethered Iridium Catalysts. *ChemCatChem* **2013**, *5* (7), 1769–1771. https://doi.org/10.1002/cctc.201200839.

(17) Luk, H. T.; Novak, G.; Safonova, O. V.; Siol, S.; Stewart, J. A.; Curulla Ferré, D.; Mondelli, C.; Pérez-Ramírez, J. CO_2-Promoted Catalytic Process Forming Higher Alcohols with Tunable Nature at Record Productivity. *ChemCatChem* **2020**, *12* (10), 2732–2744. https://doi.org/10.1002/cctc.202000059.

(18) Dorner, R. W.; Hardy, D. R.; Williams, F. W.; Willauer, H. D. Heterogeneous Catalytic CO2 Conversion to Value-Added Hydrocarbons. *Energy Environ. Sci.* **2010**, *3* (7), 884–890. https://doi.org/10.1039/c001514h.

(19) Rodemerck, U.; Holeňa, M.; Wagner, E.; Smejkal, Q.; Barkschat, A.; Baerns, M. Catalyst Development for CO_2 Hydrogenation to Fuels. *ChemCatChem* **2013**, *5* (7), 1948–1955.

https://doi.org/10.1002/cctc.201200879.

(20) Wang, Y.; Gao, W.; Kazumi, S.; Li, H.; Yang, G.; Tsubaki, N. Direct and Oriented Conversion of CO_2 into Value-Added Aromatics. *Chem. - A Eur. J.* **2019**, *25* (20), 5149–5153. https://doi.org/10.1002/chem.201806165.

(21) Li, Z.; Wang, J.; Qu, Y.; Liu, H.; Tang, C.; Miao, S.; Feng, Z.; An, H.; Li, C. Highly Selective Conversion of Carbon Dioxide to Lower Olefins. *ACS Catal.* **2017**, *7* (12), 8544–8548. https://doi.org/10.1021/acscatal.7b03251.

(22) Gao, P.; Dang, S.; Li, S.; Bu, X.; Liu, Z.; Qiu, M.; Yang, C.; Wang, H.; Zhong, L.; Han, Y.; Liu, Q.; Wei, W.; Sun, Y. Direct Production of Lower Olefins from CO2 Conversion via Bifunctional Catalysis. *ACS Catal.* **2018**, *8* (1), 571–578. https://doi.org/10.1021/acscatal.7b02649.

(23) Li, W.; Wang, H.; Jiang, X.; Zhu, J.; Liu, Z.; Guo, X.; Song, C. A Short Review of Recent Advances in CO_2 Hydrogenation to Hydrocarbons over Heterogeneous Catalysts. *RSC Adv.* **2018**, *8* (14), 7651–7669. https://doi.org/10.1039/c7ra13546g.

(24) Ojelade, O. A.; Zaman, S. F. A Review on CO_2 Hydrogenation to Lower Olefins: Understanding the Structure-Property Relationships in Heterogeneous Catalytic Systems. *J. CO2 Util.* **2021**, *47*, 101506. https://doi.org/10.1016/j.jcou.2021.101506.

(25) Corma, A.; Melo, F. V.; Sauvanaud, L.; Ortega, F. Light Cracked Naphtha Processing: Controlling Chemistry for Maximum Propylene Production. *Catal. Today* **2005**, *107–108*, 699–706. https://doi.org/10.1016/j.cattod.2005.07.109.

(26) Sattler, J. J. H. B.; Ruiz-Martinez, J.; Santillan-Jimenez, E.; Weckhuysen, B. M. Catalytic Dehydrogenation of Light Alkanes on Metals and Metal Oxides. *Chem. Rev.* **2014**, *114*

(20), 10613–10653. https://doi.org/10.1021/cr5002436.

(27) Tian, P.; Wei, Y.; Ye, M.; Liu, Z. Methanol to Olefins (MTO): From Fundamentals to Commercialization. *ACS Catal.* **2015**, *5* (3), 1922–1938. https://doi.org/10.1021/acscatal.5b00007.

(28) Stöcker, M. Methanol-to-Hydrocarbons: Catalytic Materials and Their Behavior. *Microporous Mesoporous Mater.* **1999**, *29* (1–2), 3–48. https://doi.org/10.1016/S1387-1811(98)00319-9.

(29) Goud, D.; Gupta, R.; Maligal-Ganesh, R.; Peter, S. C. Review of Catalyst Design and Mechanistic Studies for the Production of Olefins from Anthropogenic CO_2. *ACS Catal.* **2020**, *10* (23), 14258–14282. https://doi.org/10.1021/acscatal.0c03799.

(30) Zhou, W.; Cheng, K.; Kang, J.; Zhou, C.; Subramanian, V.; Zhang, Q.; Wang, Y. New Horizon in C_1 Chemistry: Breaking the Selectivity Limitation in Transformation of Syngas and Hydrogenation of CO_2 into Hydrocarbon Chemicals and Fuels. *Chem. Soc. Rev.* **2019**, *48* (12), 3193–3228. https://doi.org/10.1039/C8CS00502H.

(31) Zhang, Z.; Yin, H.; Yu, G.; He, S.; Kang, J.; Liu, Z.; Cheng, K.; Zhang, Q.; Wang, Y. Selective Hydrogenation of CO_2 and CO into Olefins over Sodium- and Zinc-Promoted Iron Carbide Catalysts. *J. Catal.* **2021**, *395*, 350–361. https://doi.org/10.1016/j.jcat.2021.01.036.

(32) Ronda-Lloret, M.; Rothenberg, G.; Shiju, N. R. A Critical Look at Direct Catalytic Hydrogenation of Carbon Dioxide to Olefins. *ChemSusChem* **2019**, *12* (17), 3896–3914. https://doi.org/10.1002/cssc.201900915.

(33) Liu, R.; Leshchev, D.; Stavitski, E.; Juneau, M.; Agwara, J. N.; Porosoff, M. D. Selective

Hydrogenation of CO_2 and CO over Potassium Promoted Co/ZSM-5. *Appl. Catal. B Environ.* **2021**, *284*, 119787. https://doi.org/10.1016/j.apcatb.2020.119787.

(34) Wang, J.; You, Z.; Zhang, Q.; Deng, W.; Wang, Y. Synthesis of Lower Olefins by Hydrogenation of Carbon Dioxide over Supported Iron Catalysts. *Catal. Today* **2013**, *215*, 186–193. https://doi.org/10.1016/j.cattod.2013.03.031.

(35) Zhang, P.; Han, F.; Yan, J.; Qiao, X.; Guan, Q.; Li, W. N-Doped Ordered Mesoporous Carbon (N-OMC) Confined Fe_3O_4-FeC_x Heterojunction for Efficient Conversion of CO_2 to Light Olefins. *Appl. Catal. B Environ.* **2021**, *299* (July), 120639. https://doi.org/10.1016/j.apcatb.2021.120639.

(36) Wu, T.; Lin, J.; Cheng, Y.; Tian, J.; Wang, S.; Xie, S.; Pei, Y.; Yan, S.; Qiao, M.; Xu, H.; Zong, B. Porous Graphene-Confined Fe-K as Highly Efficient Catalyst for CO_2 Direct Hydrogenation to Light Olefins. *ACS Appl. Mater. Interfaces* **2018**, *10* (28), 23439–23443. https://doi.org/10.1021/acsami.8b05411.

(37) Ramirez, A.; Ould-Chikh, S.; Gevers, L.; Chowdhury, A. D.; Abou-Hamad, E.; Aguilar-Tapia, A.; Hazemann, J.; Wehbe, N.; Al Abdulghani, A. J.; Kozlov, S. M.; Cavallo, L.; Gascon, J. Tandem Conversion of CO_2 to Valuable Hydrocarbons in Highly Concentrated Potassium Iron Catalysts. *ChemCatChem* **2019**, *11* (12), 2879–2886. https://doi.org/10.1002/cctc.201900762.

(38) Dorner, R. W.; Hardy, D. R.; Williams, F. W.; Willauer, H. D. K and Mn Doped Iron-Based CO_2 Hydrogenation Catalysts: Detection of $KAlH_4$ as Part of the Catalyst's Active Phase. *Appl. Catal. A Gen.* **2010**, *373* (1–2), 112–121. https://doi.org/10.1016/j.apcata.2009.11.005.

(39) Wang, X.; Wu, D.; Zhang, J.; Gao, X.; Ma, Q.; Fan, S.; Zhao, T.-S. Highly Selective Conversion of CO_2 to Light Olefins via Fischer-Tropsch Synthesis over Stable Layered K–Fe–Ti Catalysts. *Appl. Catal. A Gen.* **2019**, *573*, 32–40. https://doi.org/10.1016/j.apcata.2019.01.005.

(40) Liu, B.; Geng, S.; Zheng, J.; Jia, X.; Jiang, F.; Liu, X. Unravelling the New Roles of Na and Mn Promoter in CO_2 Hydrogenation over Fe_3O_4 -Based Catalysts for Enhanced Selectivity to Light α-Olefins. *ChemCatChem* **2018**, *10* (20), 4718–4732. https://doi.org/10.1002/cctc.201800782.

(41) Cheng, Y.; Lin, J.; Wu, T.; Wang, H.; Xie, S.; Pei, Y.; Yan, S.; Qiao, M.; Zong, B. Mg and K Dual-Decorated Fe-on-Reduced Graphene Oxide for Selective Catalyzing CO Hydrogenation to Light Olefins with Mitigated CO_2 Emission and Enhanced Activity. *Appl. Catal. B Environ.* **2017**, *204*, 475–485. https://doi.org/10.1016/j.apcatb.2016.11.058.

(42) Visconti, C. G.; Martinelli, M.; Falbo, L.; Infantes-Molina, A.; Lietti, L.; Forzatti, P.; Iaquaniello, G.; Palo, E.; Picutti, B.; Brignoli, F. CO_2 Hydrogenation to Lower Olefins on a High Surface Area K-Promoted Bulk Fe-Catalyst. *Appl. Catal. B Environ.* **2017**, *200*, 530–542. https://doi.org/10.1016/j.apcatb.2016.07.047.

(43) Visconti, C. G.; Martinelli, M.; Falbo, L.; Fratalocchi, L.; Lietti, L. CO_2 Hydrogenation to Hydrocarbons over Co and Fe-Based Fischer-Tropsch Catalysts. *Catal. Today* **2016**, *277*, 161–170. https://doi.org/10.1016/j.cattod.2016.04.010.

(44) Zhang, J.; Lu, S.; Su, X.; Fan, S.; Ma, Q.; Zhao, T. Selective Formation of Light Olefins from CO_2 Hydrogenation over Fe–Zn–K Catalysts. *J. CO2 Util.* **2015**, *12*, 95–100. https://doi.org/10.1016/j.jcou.2015.05.004.

(45) Hu, B.; Frueh, S.; Garces, H. F.; Zhang, L.; Aindow, M.; Brooks, C.; Kreidler, E.; Suib, S. L. Selective Hydrogenation of CO_2 and CO to Useful Light Olefins over Octahedral Molecular Sieve Manganese Oxide Supported Iron Catalysts. *Appl. Catal. B Environ.* **2013**, *132–133*, 54–61. https://doi.org/10.1016/j.apcatb.2012.11.003.

(46) Xu, L.; Wang, Q.; Liang, D.; Wang, X.; Lin, L.; Cui, W.; Xu, Y. The Promotions of MnO and K_2O to Fe/Silicalite-2 Catalyst for the Production of Light Alkenes from CO_2 Hydrogenation. *Appl. Catal. A Gen.* **1998**, *173* (1), 19–25. https://doi.org/10.1016/S0926-860X(98)00141-0.

(47) Xu, Q.; Xu, X.; Fan, G.; Yang, L.; Li, F. Unveiling the Roles of Fe-Co Interactions over Ternary Spinel-Type $ZnCo_xFe_{2-X}O_4$ Catalysts for Highly Efficient CO_2 Hydrogenation to Produce Light Olefins. *J. Catal.* **2021**, *400*, 355–366. https://doi.org/10.1016/j.jcat.2021.07.002.

(48) Yuan, F.; Zhang, G.; Zhu, J.; Ding, F.; Zhang, A.; Song, C.; Guo, X. Boosting Light Olefin Selectivity in CO_2 Hydrogenation by Adding Co to Fe Catalysts within Close Proximity. *Catal. Today* **2021**, *371* (August 2020), 142–149. https://doi.org/10.1016/j.cattod.2020.07.072.

(49) Numpilai, T.; Chanlek, N.; Poo-Arporn, Y.; Cheng, C. K.; Siri-Nguan, N.; Sornchamni, T.; Chareonpanich, M.; Kongkachuichay, P.; Yigit, N.; Rupprechter, G.; Limtrakul, J.; Witoon, T. Tuning Interactions of Surface-adsorbed Species over Fe−Co/K−Al_2O_3 Catalyst by Different K Contents: Selective CO_2 Hydrogenation to Light Olefins. *ChemCatChem* **2020**, *12* (12), 3306–3320. https://doi.org/10.1002/cctc.202000347.

(50) Satthawong, R.; Koizumi, N.; Song, C.; Prasassarakich, P. Light Olefin Synthesis from

CO_2 Hydrogenation over K-Promoted Fe–Co Bimetallic Catalysts. *Catal. Today* **2015**, *251*, 34–40. https://doi.org/10.1016/j.cattod.2015.01.011.

(51) Guo, L.; Cui, Y.; Li, H.; Fang, Y.; Prasert, R.; Wu, J.; Yang, G.; Yoneyama, Y.; Tsubaki, N. Selective Formation of Linear-Alpha Olefins (LAOs) by CO_2 Hydrogenation over Bimetallic Fe/Co-Y Catalyst. *Catal. Commun.* **2019**, *130*, 105759. https://doi.org/10.1016/j.catcom.2019.105759.

(52) Gong, W.; Ye, R.-P.; Ding, J.; Wang, T.; Shi, X.; Russell, C. K.; Tang, J.; Eddings, E. G.; Zhang, Y.; Fan, M. Effect of Copper on Highly Effective Fe-Mn Based Catalysts during Production of Light Olefins via Fischer-Tropsch Process with Low CO_2 Emission. *Appl. Catal. B Environ.* **2020**, *278*, 119302. https://doi.org/10.1016/j.apcatb.2020.119302.

(53) Choi, Y. H.; Jang, Y. J.; Park, H.; Kim, W. Y.; Lee, Y. H.; Choi, S. H.; Lee, J. S. Carbon Dioxide Fischer-Tropsch Synthesis: A New Path to Carbon-Neutral Fuels. *Appl. Catal. B Environ.* **2017**, *202*, 605–610. https://doi.org/10.1016/j.apcatb.2016.09.072.

(54) Xu, Y.; Li, X.; Gao, J.; Wang, J.; Ma, G.; Wen, X.; Yang, Y.; Li, Y.; Ding, M. A Hydrophobic FeMn@Si Catalyst Increases Olefins from Syngas by Suppressing C_1 By-Products. *Science (80-.).* **2021**, *371* (6529), 610–613. https://doi.org/10.1126/science.abb3649.

(55) Zhao, M.; Yan, C.; Jinchang, S.; Qianwen, Z. Modified Iron Catalyst for Direct Synthesis of Light Olefin from Syngas. *Catal. Today* **2018**, *316*, 142–148. https://doi.org/10.1016/j.cattod.2018.05.018.

(56) Li, S.; Li, A.; Krishnamoorthy, S.; Iglesia, E. Effects of Zn, Cu, and K Promoters on the Structure and on the Reduction, Carburization, and Catalytic Behavior of Iron-Based

Fischer-Tropsch Synthesis Catalysts. *Catal. Letters* **2001**, *77* (4), 197–205. https://doi.org/10.1023/A:1013284217689.

(57) Gnanamani, M. K.; Hamdeh, H. H.; Shafer, W. D.; Hopps, S. D.; Davis, B. H. Hydrogenation of Carbon Dioxide over Iron Carbide Prepared from Alkali Metal Promoted Iron Oxalate. *Appl. Catal. A Gen.* **2018**, *564*, 243–249. https://doi.org/10.1016/j.apcata.2018.07.034.

(58) Shafer, W. D.; Jacobs, G.; Graham, U. M.; Hamdeh, H. H.; Davis, B. H. Increased CO_2 Hydrogenation to Liquid Products Using Promoted Iron Catalysts. *J. Catal.* **2019**, *369*, 239–248. https://doi.org/10.1016/j.jcat.2018.11.001.

(59) Ordomsky, V. V.; Luo, Y.; Gu, B.; Carvalho, A.; Chernavskii, P. A.; Cheng, K.; Khodakov, A. Y. Soldering of Iron Catalysts for Direct Synthesis of Light Olefins from Syngas under Mild Reaction Conditions. *ACS Catal.* **2017**, *7* (10), 6445–6452. https://doi.org/10.1021/acscatal.7b01307.

(60) Peron, D. V.; Barrios, A. J.; Taschin, A.; Dugulan, I.; Marini, C.; Gorni, G.; Moldovan, S.; Koneti, S.; Wojcieszak, R.; Thybaut, J. W.; Virginie, M.; Khodakov, A. Y. Active Phases for High Temperature Fischer-Tropsch Synthesis in the Silica Supported Iron Catalysts Promoted with Antimony and Tin. *Appl. Catal. B Environ.* **2021**, *292*, 120141. https://doi.org/10.1016/j.apcatb.2021.120141.

(61) Gu, B.; Peron, D. V.; Barrios, A. J.; Bahri, M.; Ersen, O.; Vorokhta, M.; Šmíd, B.; Banerjee, D.; Virginie, M.; Marceau, E.; Wojcieszak, R.; Ordomsky, V. V.; Khodakov, A. Y. Mobility and Versatility of the Liquid Bismuth Promoter in the Working Iron Catalysts for Light Olefin Synthesis from Syngas. *Chem. Sci.* **2020**, *11* (24), 6167–6182.

https://doi.org/10.1039/D0SC01600D.

(62) Farrusseng, D. High-Throughput Heterogeneous Catalysis. *Surf. Sci. Rep.* **2008**, *63* (11), 487–513. https://doi.org/10.1016/j.surfrep.2008.09.001.

(63) Senkan, S. Combinatorial Heterogeneous Catalysis—A New Path in an Old Field. *Angew. Chemie Int. Ed.* **2001**, *40* (2), 312–329. https://doi.org/10.1002/1521-3773(20010119)40:2<312::AID-ANIE312>3.0.CO;2-I.

(64) Senkan, S. M. High-Throughput Screening of Solid-State Catalyst Libraries. *Nature* **1998**, *394* (6691), 350–353. https://doi.org/10.1038/28575.

(65) Paul, S.; Heyte, S.; Katryniok, B.; Garcia-Sancho, C.; Maireles-Torres, P.; Dumeignil, F. REALCAT: A New Platform to Bring Catalysis to the Lightspeed. *Oil Gas Sci. Technol. – Rev. d'IFP Energies Nouv.* **2015**, *70* (3), 455–462. https://doi.org/10.2516/ogst/2014052.

(66) Barrios, A. J.; Gu, B.; Luo, Y.; Peron, D. V; Chernavskii, P. A.; Virginie, M.; Wojcieszak, R.; Thybaut, J. W.; Ordomsky, V. V; Khodakov, A. Y. Identification of Efficient Promoters and Selectivity Trends in High Temperature Fischer-Tropsch Synthesis over Supported Iron Catalysts. *Appl. Catal. B Environ.* **2020**, *273*, 119028. https://doi.org/10.1016/j.apcatb.2020.119028.

(67) Klencsár, Z. Mössbauer Spectrum Analysis by Evolution Algorithm. *Nucl. Instruments Methods Phys. Res. Sect. B Beam Interact. with Mater. Atoms* **1997**, *129* (4), 527–533. https://doi.org/10.1016/S0168-583X(97)00314-5.

(68) Wezendonk, T. A.; Santos, V. P.; Nasalevich, M. A.; Warringa, Q. S. E.; Dugulan, A. I.; Chojecki, A.; Koeken, A. C. J.; Ruitenbeek, M.; Meima, G.; Islam, H. U.; Sankar, G.; Makkee, M.; Kapteijn, F.; Gascon, J. Elucidating the Nature of Fe Species during

Pyrolysis of the Fe-BTC MOF into Highly Active and Stable Fischer-Tropsch Catalysts. *ACS Catal.* **2016**, *6* (5), 3236–3247. https://doi.org/10.1021/acscatal.6b00426.

(69) Torres Galvis, H. M.; Bitter, J. H.; Davidian, T.; Ruitenbeek, M.; Dugulan, A. I.; de Jong, K. P. Iron Particle Size Effects for Direct Production of Lower Olefins from Synthesis Gas. *J. Am. Chem. Soc.* **2012**, *134* (39), 16207–16215. https://doi.org/10.1021/ja304958u.

(70) Wang, S.; Zhai, Y.; Li, X.; Li, Y.; Wang, K. Coprecipitation Synthesis of MgO-Doped ZrO 2 Nano Powder. *J. Am. Ceram. Soc.* **2006**, *89* (11), 3577–3581. https://doi.org/10.1111/j.1551-2916.2006.01244.x.

(71) Gusain, D.; Singh, P. K.; Sharma, Y. C. Kinetic and Equilibrium Modelling of Adsorption of Cadmium on Nano Crystalline Zirconia Using Response Surface Methodology. *Environ. Nanotechnology, Monit. Manag.* **2016**, *6*, 99–107. https://doi.org/10.1016/j.enmm.2016.07.002.

(72) Su, C.; Li, J.; He, D.; Cheng, Z.; Zhu, Q. Synthesis of Isobutene from Synthesis Gas over Nanosize Zirconia Catalysts. *Appl. Catal. A Gen.* **2000**, *202* (1), 81–89. https://doi.org/10.1016/S0926-860X(00)00461-0.

(73) Zhang, Z.; Zhang, L.; Hülsey, M. J.; Yan, N. Zirconia Phase Effect in Pd/ZrO2 Catalyzed CO2 Hydrogenation into Formate. *Mol. Catal.* **2019**, *475* (May). https://doi.org/10.1016/j.mcat.2019.110461.

(74) Chernavskii, P. A.; Kazak, V. O.; Pankina, G. V.; Perfiliev, Y. D.; Li, T.; Virginie, M.; Khodakov, A. Y. Influence of Copper and Potassium on the Structure and Carbidisation of Supported Iron Catalysts for Fischer-Tropsch Synthesis. *Catal. Sci. Technol.* **2017**, *7* (11), 2325–2334. https://doi.org/10.1039/c6cy02676a.

(75) Subramanian, V.; Ordomsky, V. V.; Legras, B.; Cheng, K.; Cordier, C.; Chernavskii, P. A.; Khodakov, A. Y. Design of Iron Catalysts Supported on Carbon-Silica Composites with Enhanced Catalytic Performance in High-Temperature Fischer-Tropsch Synthesis. *Catal. Sci. Technol.* **2016**, *6* (13), 4953–4961. https://doi.org/10.1039/c6cy00060f.

(76) Mai, K.; Elder, T.; Groom, L. H.; Spivey, J. J. Fe-Based Fischer Tropsch Synthesis of Biomass-Derived Syngas: Effect of Synthesis Method. *Catal. Commun.* **2015**, *65*, 76–80. https://doi.org/10.1016/j.catcom.2015.02.027.

(77) Yu, G.; Sun, B.; Pei, Y.; Xie, S.; Yan, S.; Qiao, M.; Fan, K.; Zhang, X.; Zong, B. Fe_xO_y @C Spheres as an Excellent Catalyst for Fischer−Tropsch Synthesis. *J. Am. Chem. Soc.* **2010**, *132* (3), 935–937. https://doi.org/10.1021/ja906370b.

(78) Beasley, C.; Gnanamani, M. K.; Hamdeh, H. H.; Martinelli, M.; Davis, B. H. Effect of Gallium Additions on Reduction, Carburization and Fischer–Tropsch Activity of Iron Catalysts. *Catal. Letters* **2018**, *148* (7), 1920–1928. https://doi.org/10.1007/s10562-018-2398-0.

(79) Fellenberg, A. K.; Addad, A.; Hong, J.; Simon, P.; Kosto, Y.; Šmíd, B.; Ji, G.; Khodakov, A. Y. Iron and Copper Nanoparticles inside and Outside Carbon Nanotubes: Nanoconfinement, Migration, Interaction and Catalytic Performance in Fischer-Tropsch Synthesis. *J. Catal.* **2021**, *404*, 306–323. https://doi.org/10.1016/j.jcat.2021.09.034.

(80) Ding, J.; Huang, L.; Gong, W.; Fan, M.; Zhong, Q.; Russell, A. G.; Gu, H.; Zhang, H.; Zhang, Y.; Ye, R. P. CO_2 Hydrogenation to Light Olefins with High-Performance Fe0.30Co0.15Zr0.45K0.10O1.63. *J. Catal.* **2019**, *377*, 224–232. https://doi.org/10.1016/j.jcat.2019.07.036.

(81) Dwyer, D.; Somorjai, G. A. The Role of Readsorption in Determining the Product Distribution during CO Hydrogenation over Fe Single Crystals. *J. Catal.* **1979**, *56* (2), 249–257. https://doi.org/10.1016/0021-9517(79)90111-8.

(82) Schulz, H.; Claeys, M. Kinetic Modelling of Fischer–Tropsch Product Distributions. *Appl. Catal. A Gen.* **1999**, *186* (1–2), 91–107. https://doi.org/10.1016/S0926-860X(99)00166-0.

(83) Yang, J.; Ma, W.; Chen, D.; Holmen, A.; Davis, B. H. Fischer-Tropsch Synthesis: A Review of the Effect of CO Conversion on Methane Selectivity. *Appl. Catal. A Gen.* **2014**, *470*, 250–260. https://doi.org/10.1016/j.apcata.2013.10.061.

(84) Govender, N. S.; Botes, F. G.; de Croon, M. H. J. M.; Schouten, J. C. Mechanistic Pathway for C_{2+} Hydrocarbons over an Fe/K Catalyst. *J. Catal.* **2014**, *312*, 98–107. https://doi.org/10.1016/j.jcat.2014.01.012.

(85) Olewski, T.; Todic, B.; Nowicki, L.; Nikacevic, N.; Bukur, D. B. Hydrocarbon Selectivity Models for Iron-Based Fischer–Tropsch Catalyst. *Chem. Eng. Res. Des.* **2015**, *95*, 1–11. https://doi.org/10.1016/j.cherd.2014.12.015.